

Buckling and Fundamental Frequency Optimization of Tow-Steered Composites Using Layerwise Structural Models

Original

Buckling and Fundamental Frequency Optimization of Tow-Steered Composites Using Layerwise Structural Models / RACIONERO SANCHEZ-MAJANO, Alberto; Pagani, Alfonso. - In: AIAA JOURNAL. - ISSN 0001-1452. - (2023), pp. 1-15. [10.2514/1.J062976]

Availability:

This version is available at: 11583/2980308 since: 2023-07-14T08:10:34Z

Publisher:

AMER INST AERONAUTICS ASTRONAUTICS

Published

DOI:10.2514/1.J062976

Terms of use:

This article is made available under terms and conditions as specified in the corresponding bibliographic description in the repository

Publisher copyright

(Article begins on next page)

Buckling and Fundamental Frequency Optimization of Tow-Steered Composites Using Layerwise Structural Models

Alberto Racionero Sánchez-Majano* and Alfonso Pagani†

Polytechnic University of Turin, 10129 Turin, Italy

<https://doi.org/10.2514/1.J062976>

Variable-angle-tow (VAT) composite laminates can eventually improve the mechanical performance of lightweight structures by taking advantage of a larger design space compared to straight-fiber counterparts. Here, we provide a scalable low- to high-fidelity methodology to retrieve the tow angles that maximize the buckling load and the fundamental frequency of VAT plates. A genetic algorithm is used to solve the optimization problem in which the objective function is mimicked using a surrogate model. Both unconstrained and manufactured-constrained problems are solved. The surrogates are built with outcomes from numerical models generated by means of the Carrera unified formulation, which enables to obtain straightforwardly different degrees of accuracy by selecting the order of the structural theory employed. The results show both the validity and flexibility of the proposed design approach. It is shown that, although the optimal design fiber angle orientations are consistently similar, discrepancies in the prediction of the buckling load or fundamental frequency can be found between high-fidelity layerwise and low-to-refined equivalent-single-layer models, of which classical laminated plate or first-shear deformation theories are degenerate examples.

Nomenclature

\tilde{C}	=	material stiffness matrix, Pa
D	=	differential operator
F_{cr}	=	buckling load, N
F_τ, F_s	=	through-the-thickness expansion functions
f_1	=	fundamental frequency, Hz
K_{cr}	=	buckling load factor
K_T	=	tangent stiffness matrix
K_σ	=	geometric stiffness matrix
K_0	=	stiffness matrix
M	=	mass matrix
N_i, N_j	=	finite element shape functions
q	=	unknown nodal vector
T_0, T_1	=	fiber path angle parameters, °
u	=	displacement vector
x	=	design variables vector
β	=	polynomial coefficient vector
δ	=	virtual variation
ϵ	=	strain tensor
θ	=	fiber angle orientation, °
κ	=	curvature, m ⁻¹
ρ	=	density, kg/m ³
σ	=	stress tensor
ϕ	=	fiber path rotation angle, °
ω	=	natural frequency, rad/s

Subscripts

ext	=	external
ine	=	inertia
int	=	internal
L	=	lower bound
max	=	maximum
U	=	upper bound

Received 7 March 2023; revision received 15 April 2023; accepted for publication 17 April 2023; published online Open Access 6 June 2023. Copyright © 2023 by the American Institute of Aeronautics and Astronautics, Inc. All rights reserved. All requests for copying and permission to reprint should be submitted to CCC at www.copyright.com; employ the eISSN 1533-385X to initiate your request. See also AIAA Rights and Permissions www.aiaa.org/randp.

*Ph.D. Student, Department of Mechanical and Aerospace Engineering; alberto.racionero@polito.it.

†Associate Professor, Department of Mechanical and Aerospace Engineering; alfonso.pagani@polito.it.

I. Introduction

THE irruption of novel manufacturing techniques, such as automated fiber placement (AFP) and automated type laying (ATL), brought the emergence of new families of laminated structures, namely, variable-angle-tow (VAT) composites or variable-stiffness composites (VSC), in which fiber tows are steered conforming curvilinear paths [1]. Although VAT composites have been recently introduced, the concept has existed for over three decades. Leissa and Martin [2] studied the free vibration and buckling of straight-fiber composites having nonuniformly spaced fibers and found that these two characteristics can be improved by as much as 21 and 38%, respectively. Gürdal and Olmedo [3] proposed the VSC concept and studied its in-plane response modifying the parameters that define the varying fiber path. These analyses were conducted by means of closed-form and numerical solutions based on the classical laminated plate theory (CLPT). Similarly, Gürdal et al. [4] investigated the buckling of VAT plates for different boundary conditions and rotations of the fiber path, resulting in a parametric analysis of the influence of the fiber path parameters on the nondimensional buckling load factor. Improvements up to 19 and 80%, with regard to classic laminates, were found for the different fiber path rotation angles considered. Gürdal et al. [4] solved numerically the set of partial differential equations that govern the buckling problem and that rely on the CLPT. Raju et al. [5] also utilized the CLPT for modeling VAT structures and solved the resulting differential equations by means of the differential quadrature method (DQM) to study the prebuckling and buckling of VSC structures with general boundary conditions.

Apart from CLPT, shear deformation theories based on those by Reissner [6] and Mindlin [7] have been used to study the mechanical performance of VAT plates. Akhavan and Ribeiro [8] investigated the fundamental frequency by using the third-order shear deformation theory by Reddy [9]. Venkatachari et al. [10] analyzed VSC plates and shells considering different fiber orientations and shell shapes using the first-order shear deformation theory (FSDT). Hao et al. [11] employed FSDT to model VAT shells and coupled it with isogeometric analysis to calculate the buckling load of the analyzed structures. CLPT and FSDT are examples of equivalent-single-layer (ESL) models in which the properties are homogenized through the thickness. On the contrary, layerwise (LW) models consider each layer independently, and displacement continuity has to be imposed at the layer interface.

The optimization of composite structures has been of interest to tailor the mechanical performance of the final product, and several strategies have been proposed throughout the years. Seminal work

by Haftka and Walsh [12] introduced integer programming for the stacking sequence optimization for buckling of straight-fiber laminates. Later, Le Riche and Haftka [13] proposed an integer-valued genetic algorithm (GA) to maximize the buckling performance. Therein 0, $\pm 45^\circ$, and 90° plies were encoded in order to perform the genetic operators. Le Riche and Haftka [14] then proposed an improved version of GA for the minimum thickness design of composite laminates. The usage of GA eases the coding of manufacturing constraints gathered by Irisarri et al. [15]. However, this integer-valued GA leads to a nonconvex problem, which is cumbersome to face in structural optimization. To circumvent this issue, a strategy based on lamination parameters was derived by Fukunaga and Sekine [16]. The expressions of the lamination parameters impose constraints on the design space of the lamination parameters to determine the feasible convex region where laminate configurations exist. These expressions rely on the usage of CLPT and FSDT models. GA and lamination parameters were combined in the slice and swap method proposed by Silva et al. [17] for wing optimization. This strategy consists of two steps:

i) First, a continuous optimization provides a distribution of thickness and directional stiffness that satisfy the safety margins in a series of multidisciplinary criteria. In this step, the design variables are the shell thickness, the stringer dimensions, and the stacking sequences in terms of lamination parameters.

ii) A discrete optimization process is triggered in order to transform the previous stiffness distribution to one that satisfies all the design and manufacturing rules. For a more detailed description of the slice and swap method, the reader is referred to Ref. [17].

So far, the optimization strategies of straight-fiber laminates have been discussed. Nevertheless, these can also be applied to retrieve the optimal stacking sequence of VAT composites. Serhat and Basdogan [18] proposed a CLPT lamination parameter scheme in which the radius of curvature is calculated, ensuring the manufacturability of the plate. Because AFP machines are not restricted to generating a fixed number of fiber orientations, as in the straight-fiber case, the design variables that define the fiber paths are continuous. Thus, no encoding is needed if using GA. The optimization of VSC plates manufactured by keeping a constant curvature of the AFP machine arm was studied by Nik et al. [19]. They utilized a surrogate model to mimic the in-plane stiffness and buckling load of the VAT plates and used it as the objective function of the optimization problem, which was solved by GA. Later, Nik et al. [20] proceeded accordingly to their previous work embedding the defects that arise during the AFP process, namely, gaps and overlaps. In both studies [19,20], closed-form solutions were employed to characterize the laminate structure. Optimization of in-plane stiffness, buckling load, and mass multi-objective was investigated by Vijayachandran et al. [21]. The fiber paths were generated employing Bézier curves. In this work, the design variables were the coordinates of the Bézier curves' control points, which served as input for an artificial neural network (ANN) that mimicked the aforementioned magnitudes. Shell-like S4R Abaqus finite elements (FEs) were used to model the VAT components. Singh and Kapania [22] conducted a buckling optimization of curvilinearly stiffened VAT plates, in which the design variables were the fiber path orientation parameters of the plate and the parameters used to define the shape of the stiffeners. Particle swarm optimization (PSO) was used to find the optimal design variables. Nastran shell elements were employed to model the laminate, whereas Nastran beam elements were utilized for the curved stiffeners. Zhao and Kapania [23] performed a buckling optimization of stiffened VSC laminates with a cutout imposing maximum curvature and parallel fiber path constraints. PSO was employed to solve the optimization problem, in which the fiber orientation parameters and the position of the straight stiffeners were the design variables. FSDT and Timoshenko beam theory were used for the plate and stiffeners, respectively. Carvalho et al. [24] maximized the fundamental frequency of VAT laminates taking into account gaps arising from manufacturing and maximum curvature constraints. Gaps were included by using a modified rule of mixtures accounting for the gap area fraction within the FE area. GA was used to solve the optimization problem, and S4R Abaqus elements modeled the plate.

As the reader can appreciate, ESL models based on classical theories have been generally used to optimize the buckling load and the fundamental frequency of VAT plates. To the authors' knowledge, very little or no research has been devoted to the optimization of VAT structures modeled by an LW approach. For doing so, this paper uses the Carrera unified formulation (CUF) [25]. CUF has already been used to generate both ESL, and LW models for VAT laminates, among other applications such as peridynamics [26] and civil engineering [27]. For instance, Demasi et al. [28] used 2D ESL, Zig-Zag, and LW CUF models for the stress analysis of thick VSC laminates. Viglietti et al. [29] studied the free vibration of VAT structures using variable kinematic models. Sánchez-Majano et al. [30] investigated the stress distribution of VAT shells using both ESL and LW approaches. As expected, LW outperformed ESL when predicting transverse stresses. Moreover, geometrically nonlinear analyses of VAT plates have been performed by Pagani et al. [31] to study the vibration around nonlinear equilibrium states. Last, LW stochastic analysis concerning the failure onset and the buckling of VAT laminates has been performed in [32,33]. In the former, in-plane waviness was accounted for, whereas in the latter both in-plane waviness and fiber volume fraction variability were considered. These uncertainty defects were modeled by means of stochastic fields.

This work proposes the optimization of VAT plates modeled with CUF-based LW models. Surrogate models based on polynomials are utilized to mimic the optimization's objective function, namely, buckling load factor and fundamental frequency. The optimization problem is solved by GA. Additionally, the AFP machine turning radius is considered a manufacturing constraint. The paper is organized as follows: Section II provides the main features of VAT plates and the equations to calculate the curvature of the fiber path. Section III depicts the unified FEs used to model the laminated structures. The GA characteristics and how the surrogate model is generated are available in Sec. IV. Then, model verification and optimization results are available in Sec. V. Finally, conclusions are drawn in Sec. VI.

II. Variable-Stiffness Plates and Manufacturing Constraints

In VAT composites, a band of fibers, referred to as a course, is laid over a surface following a reference path. Different paths have been analyzed throughout the years; the most common ones are those with constant curvature and linear variation. In this work, the latter are the ones to be considered. The linear variation states that the fiber angle orientation θ varies along the x' direction and reads as

$$\theta(x') = \phi + T_0 + \frac{T_1 - T_0}{d} |x'| \quad (1)$$

where T_0 is the fiber angle at $x' = 0$, and T_1 corresponds to the fiber orientation at $x' = d$, where d is the length along which the fiber angle orientation varies and typically equals the semilength or semiwidth of the VAT plate. Note that x' can be expressed in terms of the global reference system as $x' = x \cos \phi + y \sin \phi$. Last, ϕ is the fiber path rotation angle that defines along which axis, i.e., x axis, y axis, or a combination of both, the fiber orientation varies. These parameters can be appreciated in Fig. 1. In this paper, ϕ is set equal to zero. Therefore, the x' direction coincides with the x axis and $d = a/2$.

The AFP machine turning radius has a limitation on the curvature of the laid fiber path. Otherwise, an upfolded tow or a wrinkle will generate in the placed tape. Therefore, the turning radius of the AFP head limits the fiber angle distribution of each lamina and determines whether a laminate can be manufactured or not. In this regard, it is used as an optimization constraint when aiming to optimize a certain characteristic of a VAT laminate. The most commonly extended value of the AFP turning radius is $r_{\min} = 0.635$ m. Hence, the curvature is constrained as

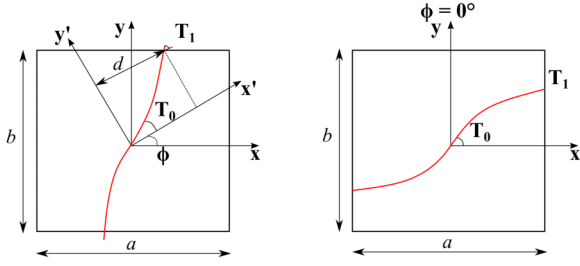


Fig. 1 Graphical representation of the parameters involved in a linearly varying fiber path for $\phi \neq 0^\circ$ (left) and $\phi = 0^\circ$ (right).

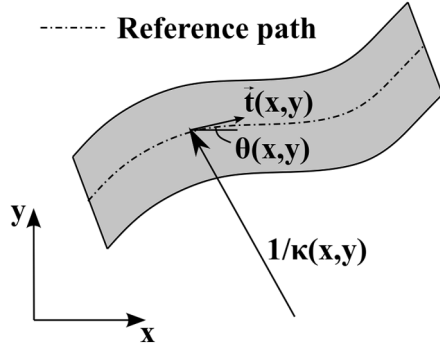


Fig. 2 Graphical representation of the tangent vector to the reference fiber path and the curvature κ at a certain (x, y) in-plane position.

$$-\frac{1}{r_{\min}} \leq \kappa \leq \frac{1}{r_{\min}} \quad (2)$$

The curvature at a specific position (x, y) can be calculated as in the work by Brooks and Martins [34], by defining the unit tangent vector \mathbf{t} (see Fig. 2) of the fiber path as

$$\mathbf{t}(\theta) = \cos(\theta)\hat{\mathbf{i}} + \sin(\theta)\hat{\mathbf{j}} \quad (3)$$

Then, performing the curl operator over vector field \mathbf{t} and keeping the only nonzero vector component yields

$$\kappa(x, y) = (\nabla \times \mathbf{t}(\theta)) \cdot \hat{\mathbf{k}} = \frac{\partial \theta}{\partial x} \cos(\theta) + \frac{\partial \theta}{\partial y} \sin(\theta) \quad (4)$$

which can be evaluated to assess whether a design is feasible from the manufacturing point of view or not. The symbols $\hat{\mathbf{i}}$, $\hat{\mathbf{j}}$, and $\hat{\mathbf{k}}$ denote the unitary vectors of a Cartesian reference frame. Note that for the case in which the fiber path varies along the x direction, i.e., $\phi = 0^\circ$, Eq. (4) reads as

$$\kappa(x) = \text{sgn}(x) \frac{T_1 - T_0}{d} \cos\left(T_0 + \frac{T_1 - T_0}{d} |x|\right) \quad (5)$$

where $\text{sgn}(\cdot)$ indicates the sign function.

III. Unified Finite Elements

Two-dimensional FEs are implemented by using the CUF formalism. According to [25], the 3D field of displacement can be expressed in terms of arbitrary through-the-thickness expansion functions $F_\tau(z)$ of the 2D generalized unknowns laying over the x - y plane; i.e.,

$$\mathbf{u}(x, y, z) = F_\tau(z) \mathbf{u}_\tau(x, y) \quad \tau = 1, \dots, M \quad (6)$$

where M is the number of expansion terms and $\mathbf{u}_\tau(x, y)$ is the vector containing the generalized displacements. Note that τ denotes summation. Common approaches for the analysis of multilayered structures are the ESL and LW approaches. In this paper, ESL models are

obtained using Taylor polynomials as F_τ along the thickness direction. On the other hand, LW makes use of Lagrange polynomials over the single layers and then imposes the displacement continuity at the interfaces; see [35,36]. In this regard, TE n indicates a TE of n th order, while LE n represents the usage of an LE with n th-order polynomials. Moreover, X LE n denotes the usage of X Lagrange polynomials of n th order to describe each layer of the laminate.

Utilizing the FE and shape functions $N_i(x, y)$, the displacement field becomes

$$\mathbf{u}_\tau(x, y) = N_i(x, y) F_\tau(z) \mathbf{q}_{\tau i} \quad i = 1, \dots, N_n \quad (7)$$

where $\mathbf{q}_{\tau i}$ denotes the unknown nodal variables, and N_n indicates the number of nodes per element. Two-dimensional nine-node quadratic, Q9, elements are employed as N_i for the x - y plane discretization.

The principle of virtual displacements (PVDs) is used to derive the governing equations of the FE model. The PVD states that the virtual variation of the internal strain energy δL_{int} has to be equal to the virtual work of the external forces δL_{ext} minus the virtual work of the inertia forces δL_{ine} ; i.e.,

$$\delta L_{\text{int}} = \delta L_{\text{ext}} - \delta L_{\text{ine}} \quad (8)$$

which in the case of free vibration analysis becomes

$$\delta L_{\text{int}} + \delta L_{\text{ine}} = 0 \quad (9)$$

The virtual variation of the strain energy can be calculated as

$$\delta L_{\text{int}} = \int_V \delta \mathbf{e}^T \boldsymbol{\sigma} dV \quad (10)$$

while the virtual work of the inertia forces is computed as

$$\delta L_{\text{ine}} = \int_V \rho \delta \mathbf{u}^T \ddot{\mathbf{u}} dV \quad (11)$$

where ρ represents the mass density of the material. Equation (10) can be rewritten using Eq. (7), the constitutive law $\boldsymbol{\sigma} = \mathbf{C}\mathbf{e}$, and the geometrical relations between strains and displacements, thus yielding

$$\delta L_{\text{int}} = \delta \mathbf{q}_{sj}^T \left[\int_V \mathbf{D}^T (N_j F_s) \bar{\mathbf{C}} \mathbf{D} (N_i F_\tau) dV \right] \mathbf{q}_{\tau i} = \delta \mathbf{q}_{sj}^T \mathbf{k}_0^{ijrs} \mathbf{q}_{\tau i} \quad (12)$$

where \mathbf{k}_0^{ijrs} is the 3×3 fundamental nucleus (FN) of the stiffness matrix, which is invariant to the order of the 2D shape functions and the through-the-thickness expansion, as shown in [25]. $\mathbf{D}(\cdot)$ is the differential operator matrix containing the geometrical relations, and $\bar{\mathbf{C}}$ is the material stiffness matrix expressed in the global reference frame, i.e., $\bar{\mathbf{C}} = \mathbf{T}(x, y) \mathbf{C} \mathbf{T}^T(x, y)$. Note the dependency of the rotation matrix \mathbf{T} on the in-plane coordinates due to the VAT fiber paths; see [32].

The virtual work of the inertia forces can be expressed as

$$\delta L_{\text{ine}} = \delta \mathbf{q}_{sj}^T \left[\int_V \rho \mathbf{I} F_\tau F_s N_i N_j dV \right] \ddot{\mathbf{q}}_{\tau i} = \delta \mathbf{q}_{sj}^T \mathbf{m}^{ijrs} \ddot{\mathbf{q}}_{\tau i} \quad (13)$$

in which \mathbf{I} is the 3×3 identity matrix and \mathbf{m}^{ijrs} is the 3×3 FN of the mass matrix. Note that \mathbf{m}^{ijrs} is a diagonal matrix.

The undamped free vibration problem can be written as follows:

$$\mathbf{M} \ddot{\mathbf{q}} + \mathbf{K}_0 \mathbf{q} = 0 \quad (14)$$

Equation (14) is obtained by looping over the FN's through the indices i, j, τ , and s to obtain the mass and stiffness matrices for the single element. Then, proceeding accordingly for the rest of FE, one can assemble the overall matrix and stiffness matrices \mathbf{M} and \mathbf{K}_0 ,

respectively. If one imposes harmonic solutions $\mathbf{q} = \tilde{\mathbf{q}}e^{i\omega t}$, then Eq. (14) turns into the following eigenvalue problem:

$$(\mathbf{K}_0 - \omega_i^2 \mathbf{M})\tilde{\mathbf{q}}_i = 0 \quad (15)$$

where ω_i and $\tilde{\mathbf{q}}_i$ are the i th natural frequency and eigenvector, respectively.

The buckling analysis consists in solving the equation

$$|\mathbf{K}_T| = 0 \quad (16)$$

where \mathbf{K}_T is the tangent stiffness matrix of the structure. The formula for this matrix is derived by means of linearizing the virtual variation of the internal strain energy:

$$\delta^2(L_{\text{int}}) = \int_V \delta(\delta \mathbf{e}^T \boldsymbol{\sigma}) dV = \int_V [\delta(\delta \mathbf{e}^T) \boldsymbol{\sigma} + \delta \mathbf{e}^T \delta \boldsymbol{\sigma}] dV \quad (17)$$

After introducing Eq. (7), the constitutive law, and the geometrical relations between strains and displacements, the previous equation adopts the following form:

$$\delta^2(L_{\text{int}}) = \delta \mathbf{q}_s^T \mathbf{k}_T^{ijrs} \delta \mathbf{q}_{ti} \quad (18)$$

This equation can be written in the case of linearized buckling problem as

$$\delta^2(L_{\text{int}}) \approx \delta \mathbf{q}_s^T (\mathbf{k}_0^{ijrs} + \mathbf{k}_\sigma^{ijrs}) \mathbf{q}_{ti} \quad (19)$$

where $\mathbf{k}_T^{ijrs} \approx \mathbf{k}_0^{ijrs} + \mathbf{k}_\sigma^{ijrs}$. Therein, \mathbf{k}_σ^{ijrs} corresponds to the 3×3 FN of the geometric stiffness matrix, which strictly depends on the internal stress state of the structure. Note that the stress state will be dependent on the accuracy of the model. The equations that allow the calculation of the tangent stiffness matrix are not reported in the paper for the sake of brevity but can be found in [37]. Last, since the linear hypothesis holds, \mathbf{k}_σ^{ijrs} is supposed to be proportional to λ_{cr} , which is the solution to a linear eigenvalue problem and is proportional to the applied load in the case of linearized buckling. Therefore, after the FN's are expanded and the elemental stiffness matrices assembled over the entire structural domain, Eq. (16) can be rewritten as follows:

$$|\mathbf{K}_0 + \lambda_{\text{cr}} \mathbf{K}_\sigma| = 0 \quad (20)$$

to calculate λ_{cr} . Note that \mathbf{K}_σ denotes the assembled geometric stiffness matrix of the structure.

The assembly of \mathbf{K}_0 , \mathbf{M} , and \mathbf{K}_σ differs whether an ESL or LW approach is chosen. In ESL, the homogenization of the properties of each layer is carried out and summed altogether when computing the stiffness matrix. As addressed by Carrera [38], ESLs do not fulfill the C_z^0 requirements. Conversely, LW considers each layer independently and expands the displacement field within each lamina. Consequently, the continuity of displacements has to be imposed at the interface (see [35,36]), thus guaranteeing the completion of the C_z^0 requirements. These two assembly approaches are displayed in Fig. 3

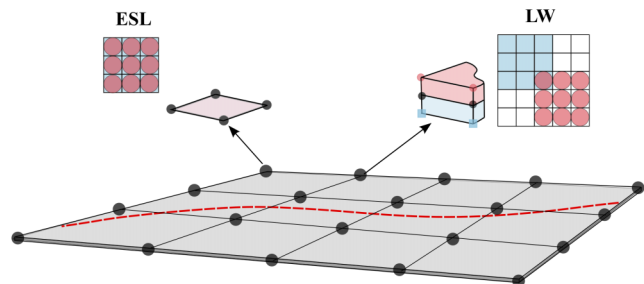


Fig. 3 Assembly procedures for ESL and LW models, and graphical representation of the displacement variable through the thickness of the plate. Straight lines represent the boundaries of the four-node FE.

for the case of a plate concerning two layers. Last, an additional feature of the proposed VAT modeling is that the fiber angle orientation is calculated at each integration point of the numerical model. This permits a more accurate description of the fiber variability and allows reducing the number of FE if compared to commercial software, as already addressed by the authors in [30].

IV. Optimization Problem

The VAT literature has demonstrated that this kind of laminates can tailor the in-plane stress resultants [22], fundamental frequencies [24], vertical deflections [39], and thermal buckling [40], among other mechanical characteristics. Based on these studies, it is observed that multiple local peaks of the mentioned characteristics exist in terms of the fiber path angles. In this context, an optimization algorithm that allows to explore the whole design space is needed. However, to perform a thorough exploration of the design space, a vast number of function evaluations are required. This need, coupled with the complexity of the VAT models, makes the optimization of these structures a computationally intensive problem. Thus, a strategy that permits exploring the design space as well as a quick evaluation of the objective, or constraint, functions is of utmost importance. The first is obtained with the usage of GA, while the latter is solved by creating response surfaces that mimic the mentioned objective or constraint functions. These two methods are explained next.

A. Genetic Algorithm

GAs are a group of evolutionary algorithms used to solve optimization problems. They are based on Darwin's Theory of Evolution [41]. Genetic operators such as crossover, elitism, and mutation are used to generate better-performing offspring, in terms of the objective function, than their parents. A GA can be used to provide the solution to both unconstrained and constrained problems, like the one in the following equation:

$$\min_x F(\mathbf{x}) \text{ s.t. } \begin{cases} g_i(\mathbf{x}) \leq 0 & i = 1, \dots, r \\ h_j(\mathbf{x}) = 0 & j = 1, \dots, k \\ \mathbf{x}_L \leq \mathbf{x} \leq \mathbf{x}_U \end{cases} \quad (21)$$

where $F(\mathbf{x})$ is the objective function, i.e., the function that one aims to minimize, while $g_i(\mathbf{x})$ and $h_j(\mathbf{x})$ are the inequality and equality constraints, respectively; \mathbf{x}_L and \mathbf{x}_U are the lower and upper bounds of the vector containing the design variables, \mathbf{x} , respectively. In this paper, an in-house developed GA based on that presented by Montemurro et al. [42] has been used. This GA allows the user to conceive individuals with a fixed or varying number of design variables and/or layers. For conducting the optimization of laminates in which the number of layers may vary, referred to as multispecies, additional genetic operators, such as specie crossover and layer addition/deletion, have to be incorporated. Despite these additional features, in this paper the number of design variables and layers of the laminates considered is kept constant throughout the optimization process. For further information about the aforementioned features, the reader is referred to [42].

Since the objective functions considered in this paper are expensive simulations, the computational cost becomes a major challenge. Therefore, the authors resort to a surrogate model that approximates the computationally expensive simulations through a multidimensional parametric surface [43].

B. Response Surface Modeling

Surrogate models can be used to accelerate the retrieval of an optimum solution. There exists a plethora of surrogate models that can be used, ranging from polynomial expressions up to ANNs [21] or passing by polynomial chaos expansion [44], radial basis functions [45], or kriging processes [46]. Because of the limited number of design variables involved in this document, a polynomial surrogate is

considered to mimic the magnitudes that aim to be optimized. For instance, a second-order polynomial can be expressed as

$$f(\mathbf{x}) = \beta_0 + \sum_{i=1}^n \beta_i x_i + \sum_{i=1}^n \sum_{j=i+1}^n \beta_{ij} x_i x_j + \sum_{i=1}^n \beta_{ii} x_i^2 \quad (22)$$

where β_0 , β_i , and β_{ij} are the polynomial coefficients; x_i are the independent variables; and n is the number of independent variables. To fit the surrogate model to the data set, the least-squares method is used to calculate the polynomial coefficients. If, for instance, a total of N_s samples are employed to construct the surrogate model and two design variables, $n = 2$, are considered, the regression problem reads as

$$\mathbf{f} = \Psi \boldsymbol{\beta} \quad (23)$$

in which \mathbf{f} is an $N_s \times 1$ column vector containing the data samples of the function that one aims to mimic, $\boldsymbol{\beta}$ contains the coefficients of the polynomial, and Ψ is a matrix with the N_s values of the design variables, i.e.,

$$\Psi = \begin{bmatrix} 1 & x_{11} & x_{12} & x_{11}x_{12} & x_{11}^2 & x_{12}^2 \\ 1 & x_{21} & x_{22} & x_{21}x_{22} & x_{21}^2 & x_{22}^2 \\ \vdots & \vdots & \vdots & \vdots & \vdots & \vdots \\ 1 & x_{N_s,1} & x_{N_s,2} & x_{N_s,1}x_{N_s,2} & x_{N_s,1}^2 & x_{N_s,2}^2 \end{bmatrix} \quad (24)$$

which, in general, is not a square matrix [47]. Hence, the coefficient vector can be calculated as

$$\boldsymbol{\beta} = (\Psi^T \Psi)^{-1} \Psi^T \mathbf{f} \quad (25)$$

To improve the accuracy of the surrogate model, Eq. (25) is solved several times, and the coefficients are averaged. As an example, let us consider a third-order polynomial comprising two independent variables. This polynomial contains 10 terms combining those two variables. Therefore, a minimum of 10 samples ($N_s = 10$) are needed to construct the polynomial. One can generate a larger database and randomly pick the 10 samples needed to calculate $\boldsymbol{\beta}$. If this process is repeated several times, an average of $\boldsymbol{\beta}$ can be obtained, leading to a better fit of the numerical model.

V. Results

A. Buckling Verification

The presented modeling approach is verified with a reference solution provided by Gürdal et al. [4]. It consists of a 12-layered VAT plate with stacking sequence $[0 \pm (0, 50)]_{3s}$. The width a and length b of the plate are $a = b = 0.254$ m, whereas the thickness of the individual ply is $t = 0.127$ mm. The material properties are listed in Table 1, and the boundary conditions are depicted in Fig. 4. The transverse displacements are restrained at $y = \pm b/2$, while a uniform shortening $u_x = u_0$ is exerted along $x = \pm a/2$.

The first step toward the verification is conducting a convergence analysis for the in-plane 2D mesh. The chosen elements consist of

Table 1 Material properties of the VAT plate considered for the linear buckling analysis, from [4]

Parameter	Value
E_1 , GPa	181.00
$E_2 = E_3$, GPa	10.27
G_{12} , GPa	7.17
G_{23} , GPa	4.00
$\nu_{12} = \nu_{23}$	0.28

The value of G_{23} was taken from [23].

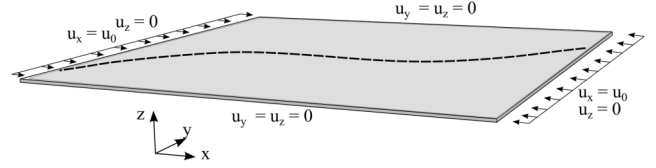


Fig. 4 Boundary conditions of the 12-layered $[0 \pm (0,50)]_{3s}$ plate.

biquadratic Lagrange polynomials, referred to as Q9 elements hereinafter, since they comprise nine nodes per element. Concerning the through-the-thickness direction, a quadratic element LE2 is utilized per each layer, providing an LW model. Convergence results are available in Table 2. These outcomes are expressed in terms of the normalized buckling load, which is computed as

$$K_{cr} = \frac{F_{cr} a^2}{E_1 h^3 b} \quad (26)$$

where h is the total thickness of the plate. It is observed that the 10×10 Q9 mesh provides a converged value of K_{cr} . The difference between the reference value [4] and the one calculated with the present methodology stems from the models employed. Gürdal et al. [4] used the CLPT and the Rayleigh–Ritz method to calculate the buckling load, whereas the proposed model utilizes an LW description of the laminated VAT plate. Clearly, CLPT offers a stiffer and more conservative solution in this case. In addition, Fig. 5 provides the convergence of the first five buckling load factors and their respective modes. It is observed that the first four modes converged within 1% for the 10×10 Q9 mesh, while the fifth one shows roughly a 3% discrepancy.

The next step involves using different expansion functions in the through-the-thickness direction. A comparison between Taylor and Lagrange expansions is shown in Table 3. These models employ the

Table 2 Convergence analysis in terms of K_{cr} for the $[0 \pm (0,50)]_{3s}$ plate from [4]

Model	DOF	K_{cr}
Ref. [4]	—	1.44
4×4 Q9	6,075	1.42
6×6 Q9	12,675	1.41
8×8 Q9	21,675	1.40
10×10 Q9	33,075	1.39
12×12 Q9	46,875	1.39
14×14 Q9	63,075	1.39

Each discretization employs 1 LE2 element per layer.

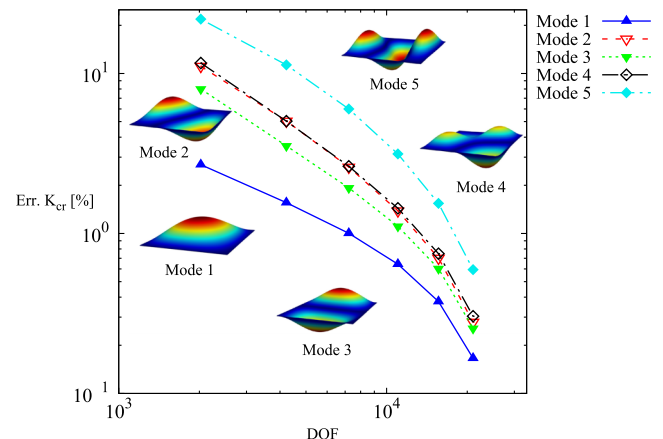


Fig. 5 Convergence of K_{cr} in terms of DOF. The first five buckling modes are illustrated.

Table 3 Convergence analysis of K_{cr} for the $[0 \pm (0,50)]_{3s}$ plate from [4]

Model	DOF	K_{cr}
Ref. [4]	—	1.44
TE 1	2,646	1.42
TE 2	3,969	1.40
TE 3	5,292	1.39
TE 4	6,615	1.39
1 LE1	17,199	1.42
1 LE2	33,075	1.39

Each model employs a 10×10 Q9 mesh.

10×10 Q9 mesh demonstrated to provide a converged solution for K_{cr} . Note that, in the current procedure, ESL models are obtained with TE polynomials. TE 1, which is similar to FSDT, provides the closest solution to the reference CLPT. Then, as the order of TE increases, lower values of K_{cr} are predicted. Indeed, the TE 3 model can obtain the same value provided by the LE2 model with an 84% reduction in terms of degrees of freedom (DOF).

B. Free Vibration Verification

The free vibration problem is verified against the results available in Akhavan and Ribeiro [8]. The study case concerns a three-layered squared plate with stacking sequence $[(0, 45), (-45, -60), (0, 45)]$. The width and length of the plate are $a = b = 1$ m, and a width-to-thickness ratio $a/h = 10$, having each ply the same thickness. The material elastic properties are reported in Table 4. The structure is fully clamped.

As performed in the previous section, a convergence of the FE mesh is done first, employing Q9 FE and LE2 in the thickness direction. The results are listed in Table 5 and illustrated in Fig. 6 along with the first five free vibration modes. A good agreement between Ref. [8] and the present results is observed. All the first five modes but the fourth one converge within 1% using the 10×10 Q9 grid. This mesh provides a higher value than the 16×16 Q9 one. However, the relative error between both solutions is 0.19%, presenting the 10×10 a twofold reduction in terms of computation time. Therefore, the 10×10 Q9 mesh will be used for the subsequent analyses.

The usage of different expansion functions in the thickness direction is now addressed. The comparison between the various

Table 4 Material properties of the VAT plate considered for the free vibration analysis, from [8]

Parameter	Value
E_1 , GPa	173.00
$E_2 = E_3$, GPa	7.20
G_{12} , GPa	3.76
G_{23} , GPa	3.76
$\nu_{12} = \nu_{23}$	0.29
ρ , kg/m ³	1540.00

Table 5 Convergence analysis of the first five natural frequencies for the $[(0,45), (-45, -60), (0,45)]$ plate from [8]

Model	DOF	f_1 , Hz	f_2 , Hz	f_3 , Hz	f_4 , Hz	f_5 , Hz
Ref. [8]	—	613.79	909.04	1,231.65	1,337.69	1,484.53
6×6 Q9	3,549	614.82	916.05	1,230.29	1,361.72	1,492.04
8×8 Q9	6,069	611.26	907.03	1,219.97	1,337.03	1,475.20
10×10 Q9	9,261	609.91	903.93	1,216.18	1,328.88	1,469.58
12×12 Q9	13,125	609.28	902.56	1,214.47	1,325.46	1,467.15
16×16 Q9	22,869	608.74	901.46	1,213.07	1,322.85	1,465.21

Each discretization employs 1 LE2 element per layer.

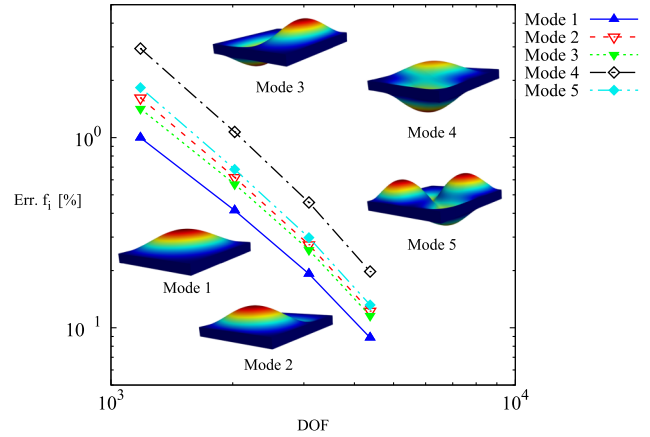


Fig. 6 Convergence of the first five fundamental frequencies in terms of DOF. The first five free vibration modes are illustrated.

TE and LE expansions is shown in Table 6. All the tested numerical models employ a 10×10 Q9 mesh. It is observed that first- and second-order TEs provide higher natural frequencies values than the reference solution. Third- and fourth-order TEs provide closer values to the reference but are still slightly higher than the LW models. Fifth- and sixth-order TEs can calculate the same solution as the 1 LE2 model employed for the FE convergence analysis. Note that TE 4 and TE 6 compute higher fifth frequencies than their TE counterparts. Last, the three different LW models, i.e., LE 1, LE 2, and LE 3, present some discrepancies among them. LE 1 provides results between TE 2 and LE 2, while LE 3 computes lower frequencies than LE 2 with an increase in both DOF and computational time. Thus, the chosen numerical model is the one comprising a 10×10 Q9 FE mesh and 1 LE 2 description through the thickness.

To show that the present methodology can handle different boundary conditions while keeping the FE mesh and the diverse structural theories that have been accounted for, simply supported boundary conditions are considered now for the $[(0,45), (-45, -60), (0,45)]$ plate. For the sake of brevity, the convergence study is not reported. The effect of structural theory is listed in Table 7. It is observed that ESL TE 1 and TE 2 overestimate the fundamental frequencies compared to Ref. [8]. If higher ESL theories are employed (see ESL-TE 3 and beyond), their prediction is in good agreement with the reference, which, indeed, uses a third-order model. However, if an LW approach is used, a more flexible structure is obtained, and thus a lower fundamental frequency is retrieved.

C. Buckling Optimization

Referring to the problem in Sec. V.A, the buckling optimization can be stated as

$$\min_{\mathbf{x}} -F_{cr}(\mathbf{x}) \quad (27)$$

in which $\mathbf{x} = \{T_0, T_1\}$ are the design variables corresponding to a laminate stacking sequence $\theta = [0 \pm \langle T_0, T_1 \rangle]_{3s}$, and F_{cr} denotes the critical buckling load. The lower and upper bounds are $\mathbf{x}_L = -90^\circ$ and $\mathbf{x}_U = 90^\circ$, respectively, as in [23,24]. To solve the optimization problem, the response surface method explained in Sec. IV.B is used to mimic the distribution of F_{cr} as a function of the variable orientation parameters T_0 and T_1 . Therefore, F_{cr} is approximated by \tilde{F}_{cr} , i.e., $F_{cr} \approx \tilde{F}_{cr}$, in Eq. (27). Note that \tilde{F}_{cr} represents the response surface model of F_{cr} . Fifteen samples were generated by means of Latin hypercube sampling (LHS) [48] to construct the surrogate model for the LW-LE2 and ESL TE1 and TE3 structural models and width-to-thickness a/h ratios. Figure 7 shows the constructed response surface and the sample data for the LW-LE2 and ESL-TE3 thin plate models, as well as their contour plot. Two local maxima are appreciated, from whom one is the

Table 6 Convergence analysis of the first five natural frequencies for the fully clamped $[(0,45), (-45, -60), (0,45)]$ plate from [8]

Model	DOF	f_1 , Hz	f_2 , Hz	f_3 , Hz	f_4 , Hz	f_5 , Hz
Ref. [8]	— —	613.79	909.04	1,231.65	1,337.69	1,484.53
TE 1	2,646	638.87 ^{4.09%}	955.51 ^{5.11%}	1,278.43 ^{3.80%}	1,419.71 ^{6.13%}	1,553.57 ^{4.65%}
TE 2	3,969	634.39 ^{3.36%}	943.64 ^{3.81%}	1,273.88 ^{3.43%}	1,399.97 ^{4.66%}	1,542.34 ^{3.89%}
TE 3	5,292	611.17 ^{-0.43%}	908.11 ^{-0.10%}	1,218.00 ^{-1.11%}	1,338.39 ^{0.05%}	1,473.10 ^{-0.70%}
TE 4	6,615	611.04 ^{-0.45%}	907.83 ^{-0.13%}	1,217.56 ^{-1.14%}	1,337.69 ^{0%}	1,789.14 ^{20.52%}
TE 5	7,938	609.49 ^{-0.70%}	903.63 ^{-0.60%}	1,214.24 ^{-1.41%}	1,328.60 ^{-0.68%}	1,467.81 ^{-1.13%}
TE 6	9,261	609.49 ^{-0.70%}	903.63 ^{-0.60%}	1,214.24 ^{-1.41%}	1,328.59 ^{-0.68%}	1,774.46 ^{19.53%}
1 LE1	5,292	621.64 ^{1.28%}	917.66 ^{0.95%}	1,244.85 ^{1.07%}	1,347.15 ^{0.71%}	1,499.66 ^{1.02%}
1 LE2	9,261	609.91 ^{-0.63%}	903.93 ^{-0.56%}	1,216.18 ^{-1.26%}	1,328.88 ^{-0.66%}	1,469.58 ^{-1.01%}
1 LE3	13,230	608.60 ^{-0.85%}	900.62 ^{-0.93%}	1,213.16 ^{-1.50%}	1,322.06 ^{-1.17%}	1,464.94 ^{-1.32%}

Each model employs a 10×10 Q9 mesh. The relative difference between each model and the reference is reported in the superscript.

Table 7 Convergence analysis of the first five natural frequencies for the simply supported $[(0,45), (-45, -60), (0,45)]$ plate from [8]

Model	DOF	f_1 , Hz	f_2 , Hz	f_3 , Hz	f_4 , Hz	f_5 , Hz
Ref. [8]	— —	467.31	746.54	1,114.80	1,166.28	1,349.00
TE 1	2,646	483.27 ^{3.41%}	782.96 ^{4.88%}	1,167.42 ^{4.72%}	1,237.37 ^{6.10%}	1,355.62 ^{0.49%}
TE 2	3,969	479.51 ^{2.61%}	771.63 ^{3.36%}	1,162.71 ^{4.30%}	1,215.46 ^{4.22%}	1,333.97 ^{-1.1%}
TE 3	5,292	466.85 ^{-0.10%}	746.81 ^{0.04%}	1,114.73 ^{-0.01%}	1,168.35 ^{0.26%}	1,348.81 ^{-0.01%}
TE 4	6,615	466.81 ^{-0.11%}	746.70 ^{0.02%}	1,114.51 ^{-0.03%}	1,169.01 ^{0.23%}	1,320.75 ^{-2.09%}
TE 5	7,938	465.36 ^{-0.42%}	742.59 ^{-0.53%}	1,112.21 ^{-0.23%}	1,160.83 ^{-0.47%}	1,320.60 ^{-2.10%}
TE 6	9,261	465.36 ^{-0.42%}	742.58 ^{-0.53%}	1,112.20 ^{-0.23%}	1,160.83 ^{-0.47%}	1,317.28 ^{-2.35%}
1 LE1	5,292	431.91 ^{-7.58%}	691.34 ^{-7.39%}	1,060.18 ^{-4.90%}	1,107.68 ^{-5.02%}	1,273.80 ^{-5.57%}
1 LE2	9,261	432.13 ^{-7.53%}	692.01 ^{-7.30%}	1,061.63 ^{-4.77%}	1,109.47 ^{-4.87%}	1,276.17 ^{-5.40%}
1 LE3	13,230	429.63 ^{-8.06%}	686.85 ^{-8.00%}	1,051.63 ^{-5.67%}	1,098.96 ^{-5.77%}	1,262.98 ^{-6.38%}

Each model employs a 10×10 Q9 mesh. The relative difference between each model and the reference is reported in the superscript.

global maximum. As one can appreciate, both response surfaces from Figs. 7a and 7c, and contour plots in 7b and 7d, are practically identical, and just slight differences in the surrogate model's coefficients are observed.

The optimization solution is obtained by employing the GA depicted in Sec. IV.A. The GA population comprises a total of 40 individuals, i.e., 20 per design variable. The crossover probability is set to 80%, whereas the mutation probability is equal to 5%. The solutions found for each modeling approach and a/h ratio are gathered in Table 8. It is appreciated that, for the thin plate case, the LW and ESL theories provide practically the same optimal value of $\langle T_0, T_1 \rangle$, with only the difference in T_0 for the ESL-TE 3 model in which $T_0 = -11.77^\circ$ instead of $T_0 = -17^\circ$. These results are in agreement with the ones presented by Gürdal et al. [4], where it was found that the maximum buckling load was achieved when $\langle T_0, T_1 \rangle = (0, 50)^\circ$. The difference between the present solution and the one in [4] resides in the range of the design variables. In this paper, the range considered is $T_0, T_1 \in [-90, 90]^\circ$, while in [4] it was $T_0, T_1 \in [0, 90]^\circ$. When thick plates are considered, LW and ESL models provide similar solutions as appreciated in Table 8. Small differences are observed in the value of T_0 . As expected, ESL provides higher values of the buckling load since they lead to stiffer models. As mentioned before, the reason why slightly different solutions are obtained resides in the surrogate model's coefficients. However, these are affected by the sample data used to construct the response surface, i.e., F_{cr} . Likewise, the eigenvalues to the buckling problem, and therefore F_{cr} , depend on the linear and geometric stiffness matrices, whose components vary according to the chosen structural model. In particular, the geometric stiffness matrix involves the stress state of the structure, which, again, varies whether an LW or an ESL is employed to model the structure as shown in Fig. 8. Therein, it is observed that for thick plates there is a vast difference when computing the in-plane normal stress σ_{xx} with LW-LE2 and

ESL-TE3 models (see Fig. 8a), whereas both theories of structures lead to practically the same distribution. Note that in reality the plate would not be able to withstand such high stress state levels without incurring into geometrical nonlinearities or failure. Those huge magnitudes stem from the fact that linear analyses have been performed. Concerning the transverse normal stress σ_{zz} displayed in Fig. 8b, the ESL-TE3 theory cannot reach the LW-LE2 maximum value for the thick plate. In the case of thin laminates, the transverse magnitudes are negligible if compared to thicker plates and an accurate evaluation of them would require the use of the mixed interpolation of tensorial components (MITC) approach [49] to circumvent the shear-locking phenomenon.

As Olmedo and Gürdal demonstrated in their seminal work [50], fiber steering leads to an increase in the buckling load compared to classical straight-fiber configurations. However, some of the designs presented in Table 8 are not feasible to manufacture due to limitations on the turning radius of the AFP machines. Therefore, a constrained optimization problem shall be faced. In this regard, the constrained buckling load optimization problem is written as

$$\min_{\mathbf{x}} -F_{cr}(\mathbf{x}) \text{ s.t. } -1/r_{\min} \leq \kappa(\mathbf{x}) \leq 1/r_{\min} \quad (28)$$

where $\kappa(\mathbf{x})$ is calculated using Eq. (5). The number of design variables and their upper and lower bounds are kept from the unconstrained buckling optimization problem. Again, the optimization problem is solved by employing the response surfaces built from the different CUF theories of structures. The optimal design variables along with the predicted \tilde{F}_{cr} , the actual F_{cr} , the relative error between them, and the maximum value of the curvature κ_{\max} are listed in Table 9 for the considered width-to-thickness ratios. As occurred for the unconstrained buckling optimization problem, LW and ESL theories provide design

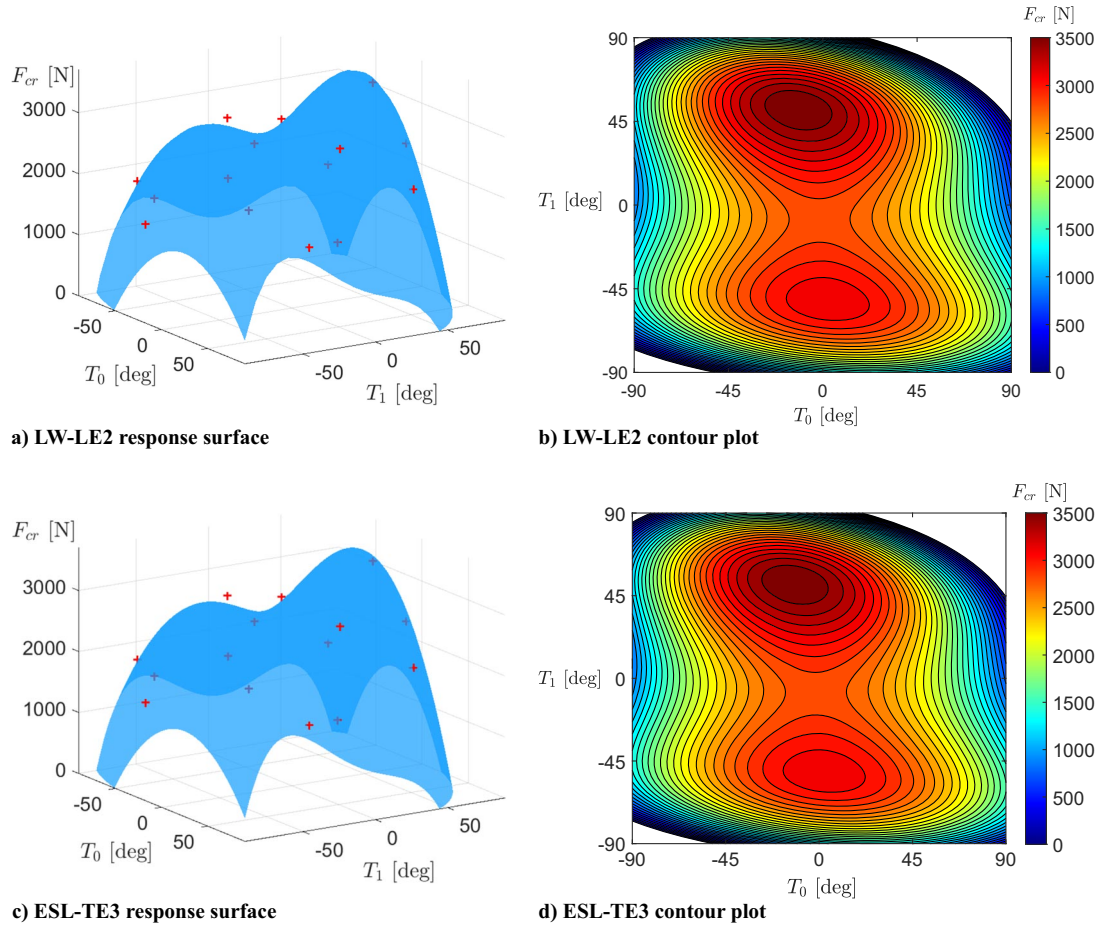


Fig. 7 Response surface and contour plot of the $[0 \pm \langle T_0, T_1 \rangle]_{3s}$ plate with width-to-thickness ratio $a/h = 167$ for the LW-LE2 and ESL-TE3 models. Red crosses in (a) and (c) indicate the sample points used to construct the surrogate models.

Table 8 Optimal results of the unconstrained buckling optimization problem for the $[0 \pm \langle T_0, T_1 \rangle]_{3s}$ plate, and comparison between surrogate model \bar{F}_{cr} and direct analysis F_{cr} of the optimized stacking sequence

Parameter	$a/h = 10$			$a/h = 167$		
	LW-LE2	ESL-TE 1	ESL-TE 3	LW-LE2	ESL-TE 1	ESL-TE 3
$\langle T_0, T_1 \rangle$	$\langle -1.90, 40.97 \rangle$	$\langle -3.38, 40.46 \rangle$	$\langle -3.37, 40.97 \rangle$	$\langle -17, 52 \rangle$	$\langle -17, 52 \rangle$	$\langle -11.77, 51.88 \rangle$
\bar{F}_{cr}, N	$8.24 \cdot 10^6$	$9.34 \cdot 10^6$	$8.73 \cdot 10^6$	$3.58 \cdot 10^3$	$3.58 \cdot 10^3$	$3.58 \cdot 10^3$
F_{cr}, N	$8.28 \cdot 10^6$	$9.37 \cdot 10^6$	$8.73 \cdot 10^6$	$3.48 \cdot 10^3$	$3.56 \cdot 10^3$	$3.33 \cdot 10^3$
Error, %	-0.51	-0.31	0.06	2.73	1.00	7.40

variables similar to each other when thin plates ($a/h = 167$ case) are modeled. The optimal design variables for the thin plate are around $\langle T_0, T_1 \rangle \approx \langle 20, 32 \rangle^\circ$. As occurred in the unconstrained problem, LW and ESL lead to the same solution when thick plates are analyzed. In this case, the optimal design variables are around $\langle T_0, T_1 \rangle \approx \langle 12, 24 \rangle^\circ$. It is appreciated that, for each of the width-to-thickness ratios and structural theories, the optimal design lays in the constraint boundary.

Some differences are appreciated between the solutions to the unconstrained and the constrained problems for both width-to-thickness ratios. First, an abrupt sign change occurs between T_0 and T_1 in the unconstrained problem, as observed in Figs. 9a and 9c, whereas a smoother fiber path is appreciated in the constrained one (see Figs. 10a and 10c). Concerning the first buckling mode, a sharper form pointing toward the left inferior and right upper corners is observed for the constrained solution in Figs. 10b and 10d, while a rounder shape is presented in the unconstrained laminate in Figs. 9b and 9d. This difference is due to the larger stiffness

close to the shortened edges in the thick $\langle T_0, T_1 \rangle = \langle 12.10, 23.83 \rangle^\circ$ and thin $\langle T_0, T_1 \rangle = \langle 20.81, 33.08 \rangle^\circ$ design compared to the thick $\langle T_0, T_1 \rangle = \langle -1.90, 40.97 \rangle^\circ$ and thin $\langle T_0, T_1 \rangle = \langle -17, 52 \rangle^\circ$ unconstrained designs.

D. Fundamental Frequency Optimization

The fundamental frequency optimization problem reads as

$$\min_{\mathbf{x}} -f_1(\mathbf{x}) \quad (29)$$

where $\mathbf{x} = \{T_0, T_1\}$ are the design variables relative to a fully clamped plate whose stacking sequence is $\theta = [0 \langle T_0, T_1 \rangle, 0 \langle 90 + T_0, 90 + T_1 \rangle]_s$, as in the work by Akhavan and Ribeiro [8]. The lower and upper bounds are $\mathbf{x}_L = -90^\circ$ and $\mathbf{x}_U = 90^\circ$, respectively. The material properties are the ones used in Sec. V.B and listed in Table 4, while the width and length of the plate are $a = b = 1$ m. Two width-to-thickness ratios are considered,

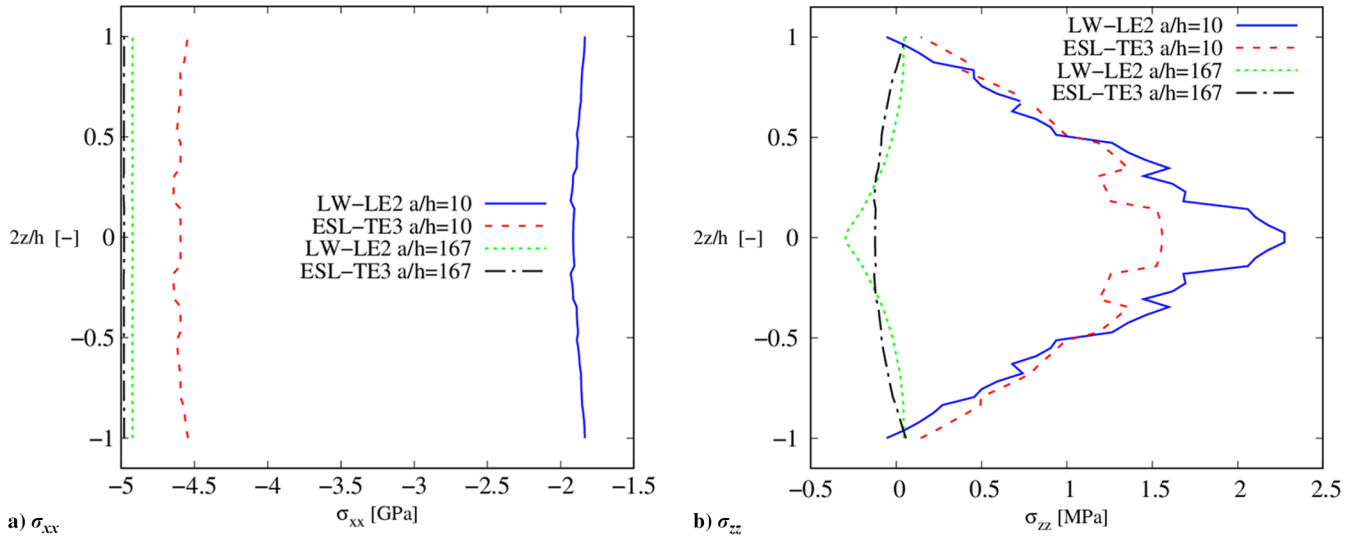


Fig. 8 Distributions of a) σ_{xx} and b) σ_{zz} for the different width-to-thickness ratios and LW-LE2 and ESL-TE3 structural theories. For both width-to-thickness ratios, their respective LW-LE2 solution from Table 8 was used to calculate the stress distributions.

Table 9 Optimal results of the constrained buckling optimization problem for the $[0 \pm \langle T_0, T_1 \rangle]_{3s}$ plate subjected to uniform end shortening and restrained transverse edges, comparison between surrogate model \tilde{F}_{cr} and direct analysis F_{cr} of the optimized stacking sequence, and maximum value of the steering curvature

Parameter	$a/h = 10$			$a/h = 167$		
	LW-LE2	ESL-TE 1	ESL-TE 3	LW-LE2	ESL-TE 1	ESL-TE 3
$\langle T_0, T_1 \rangle [^\circ]$	$\langle 12.10, 23.83 \rangle$	$\langle 9.57, 21.20 \rangle$	$\langle 12.28, 24.01 \rangle$	$\langle 20.81, 33.08 \rangle$	$\langle 17.41, 29.45 \rangle$	$\langle 18.93, 31.08 \rangle$
\tilde{F}_{cr}, N	$8.08 \cdot 10^6$	$9.14 \cdot 10^6$	$8.51 \cdot 10^6$	$3.05 \cdot 10^3$	$3.05 \cdot 10^3$	$3.15 \cdot 10^3$
F_{cr}, N	$8.08 \cdot 10^6$	$9.05 \cdot 10^6$	$8.47 \cdot 10^6$	$3.18 \cdot 10^3$	$3.20 \cdot 10^3$	$3.18 \cdot 10^3$
Error, %	0.07	1.07	0.49	-3.97	-4.84	-0.59
κ_{max}, m^{-1}	1.57	1.57	1.57	1.57	1.57	1.57

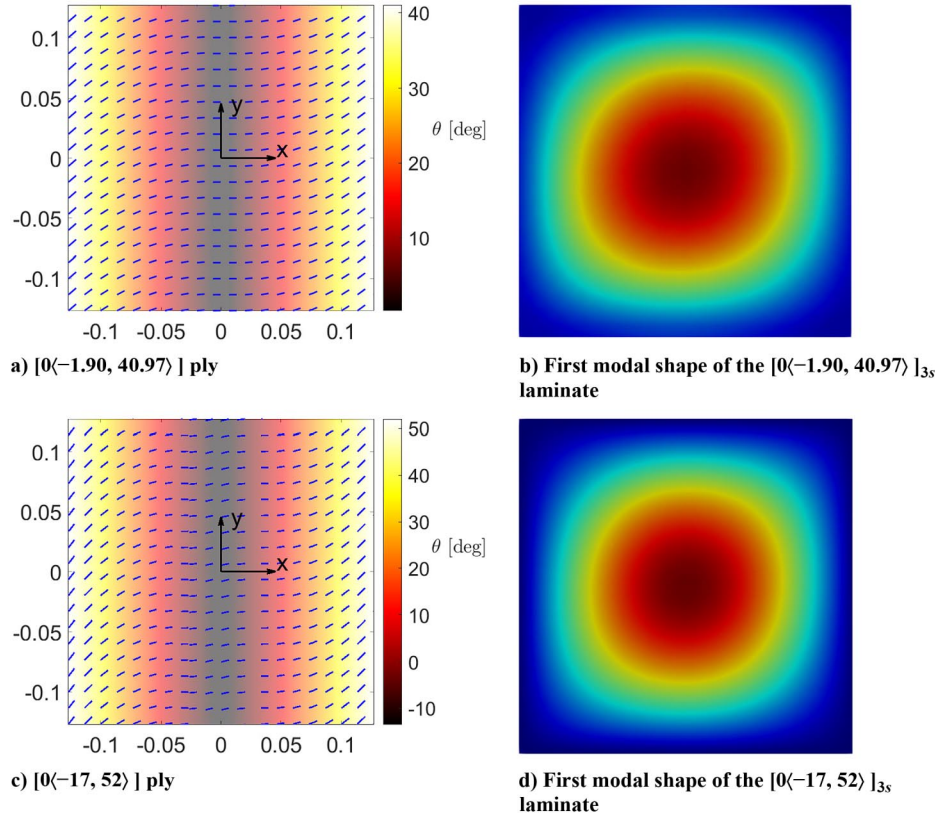


Fig. 9 Fiber paths and first buckling mode of the LW optimum solution for the unconstrained buckling load optimization problem for thick (a, b) and thin (c, d) laminates.

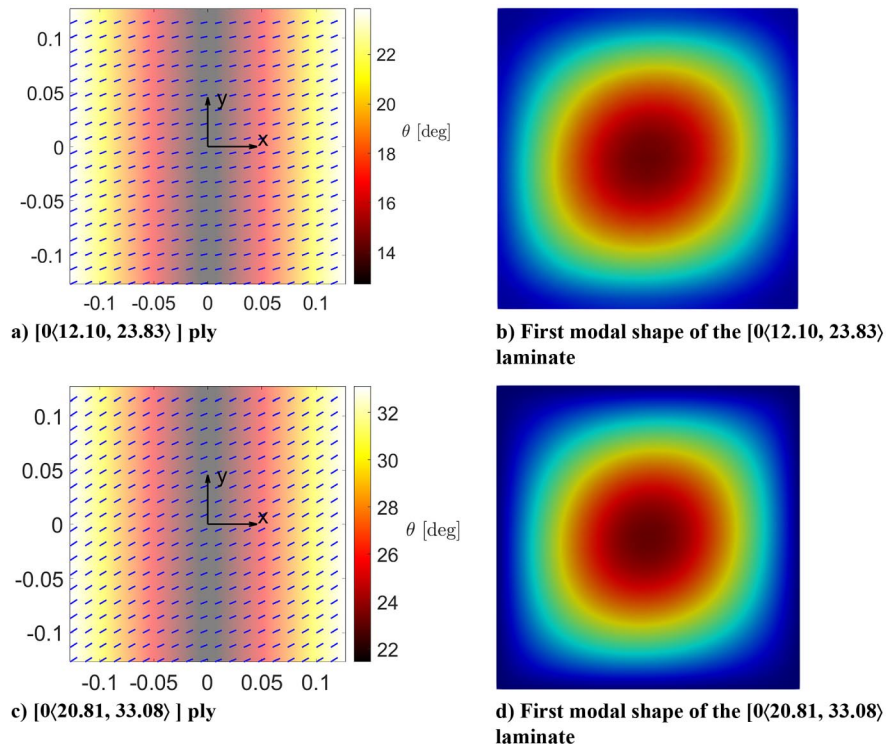


Fig. 10 Fiber paths and first buckling mode of the LW optimum solution for the constrained buckling load optimization problem for thick (a, b) and thin (c, d) laminates.

namely, $a/h = 10$ and $a/h = 100$, which represent the case of thick and thin laminates, respectively.

The effect of the structural theory on the fundamental frequency optimization results is analyzed for thick and thin laminates. The FE mesh comprises 10×10 Q9 elements with different through-the-thickness expansion functions and modeling approaches, namely, ESL-TE 1, ESL-TE 3, and LW employing an LE2 discretization. The mesh convergence analysis has been omitted for the sake of brevity.

As in Sec. V.C, the optimization problem is solved by using a surrogate model that mimics f_1 over the design space. Therefore, f_1 is approximated by \tilde{f}_1 ; i.e., $f_1 \approx \tilde{f}_1$ in Eq. (29). Likewise, 15 samples were generated by means of LHS to construct the response surface. Note that the same $\langle T_0, T_1 \rangle$ pairs are used to build the surrogate for the different structural theories and width-to-thickness ratio. All the structural models used a truncated fourth-order response surface to mimic the FE simulations. The LW response surface and its contour

plot are represented in Fig. 11. Concerning the GA parameters, 40 individuals were considered per generation, with a crossover probability equal to 80 and 5% mutation probability.

Table 10 reports the optimum design variables achieved with the various structural theories and width-to-thickness ratios for the unconstrained optimization problem. One can observe that LW and ESL provide similar solutions for both thick ($a/h = 10$) and thin ($a/h = 100$) laminates. In all of the obtained laminations, T_1 has a negative value as appreciated in Figs. 12a and 12c. In it, fibers are pointing toward the $x = \pm a/2$ edges with constant T_1 orientation. In these edges, the local elastic modulus [3] in the x directions is greater than in the middle of the plate. Conversely, the fibers point toward the $y = \pm b/2$ edges at $x = 0$, where they present the maximum transverse stiffness. This fiber pattern is in agreement with the optimization results for the fully clamped squared plate shown in Table 8 from [24]. Moreover, agreement in the negative sign of T_1 between the proposed ESL solutions and those reported in [24] is found. That

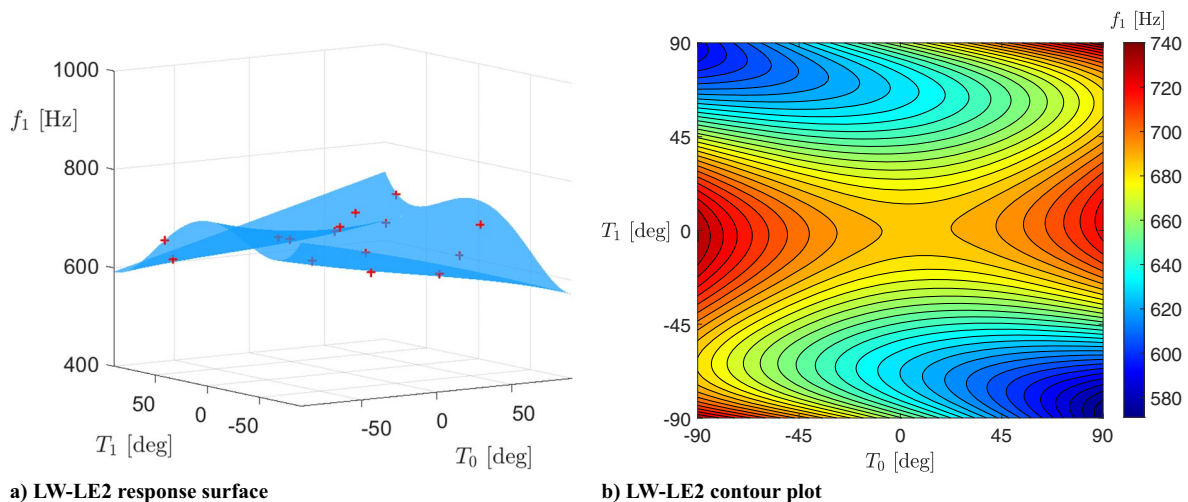
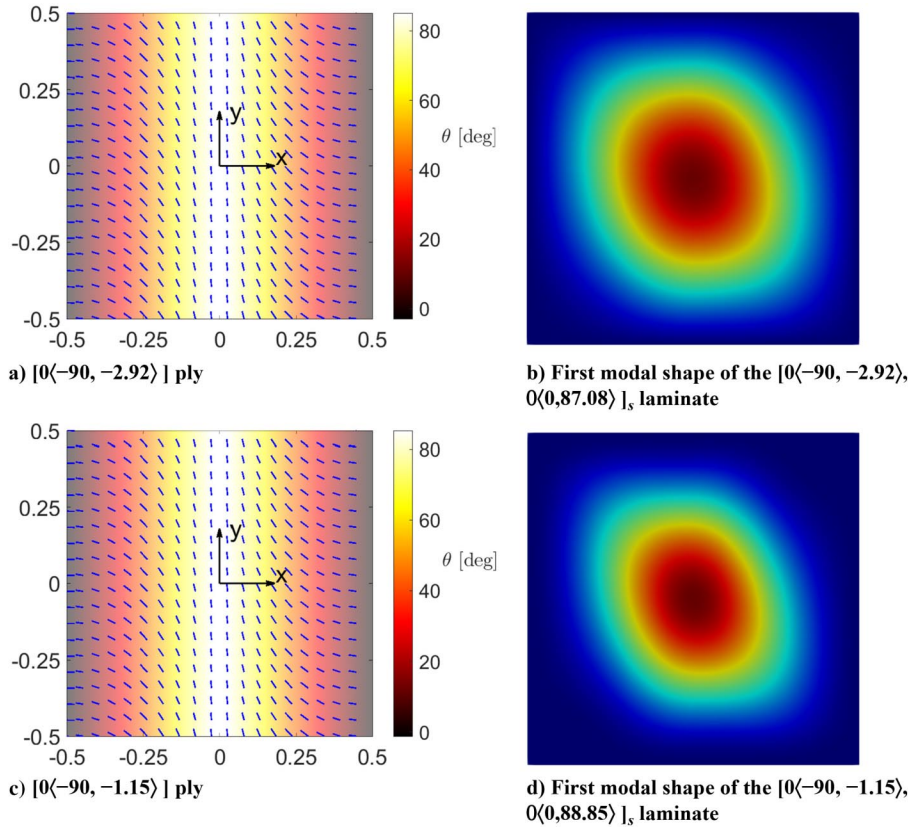


Fig. 11 Response surface and contour plot of the fully clamped $[0(T_0, T_1), 0(90 + T_0, 90 + T_1)]$ plate with width-to-thickness ratio $a/h = 10$. Red crosses in (a) indicate the sample points used to construct the surrogate models.

Table 10 Optimal results of the unconstrained first fundamental frequency optimization problem for the fully clamped $[0(T_0, T_1), 0(90 + T_0, 90 + T_1)]_s$ plate, and comparison between surrogate model \tilde{f}_1 and direct analysis f_1 of the optimized stacking sequence

Parameter	$a/h = 10$			$a/h = 100$		
	LW-LE2	ESL-TE 1	ESL-TE 3	LW-LE2	ESL-TE 1	ESL-TE 3
$\langle T_0, T_1 \rangle [^\circ]$	$\langle -90, -2.92 \rangle$	$\langle -90, -2.30 \rangle$	$\langle -90, -2.41 \rangle$	$\langle -90, -1.15 \rangle$	$\langle -90, -1.26 \rangle$	$\langle -90, -1.15 \rangle$
\tilde{f}_1 , Hz	735.23	769.86	738.96	125.48	126.51	125.60
f_1 , Hz	737.43	774.47	741.71	123.21	124.19	123.24
Error, %	-0.29	-0.59	-0.37	1.84	1.87	1.91

**Fig. 12** Fiber paths and first vibration mode of the LW optimum solution for the unconstrained fundamental frequency optimization problem for thick (a, b) and thin (c, d) laminates.

work [24] employed shell-like S4R Abaqus elements with similar capabilities as the ESL-TE 1 model used in this paper.

The curvature-constrained fundamental frequency optimization reads as

$$\min_{\mathbf{x}} -f_1(\mathbf{x}) \text{ s.t. } -1/r_{\min} \leq \kappa(\mathbf{x}) \leq 1/r_{\min} \quad (30)$$

where $\kappa(\mathbf{x})$ is calculated using Eq. (5). The optimization results are summarized in Table 11. Changes with respect to the unconstrained results are appreciated. Again, LW and ESL models provide similar results for both thick and thin laminates. The main difference is found in the prediction of the fundamental frequency for thick laminates, where ESL models lead to overestimated values of f_1 , especially

Table 11 Optimal results of the constrained first fundamental frequency optimization problem for the $[0(T_0, T_1), 0(90 + T_0, 90 + T_1)]_s$ fully clamped plate, comparison between surrogate model \tilde{f}_1 and direct analysis f_1 of the optimized stacking sequence, and maximum value of the steering curvature

Parameter	$a/h = 10$			$a/h = 100$		
	LW-LE2	ESL-TE 1	ESL-TE 3	LW-LE2	ESL-TE 1	ESL-TE 3
$\langle T_0, T_1 \rangle [^\circ]$	$\langle -90, -34.96 \rangle$	$\langle -84.68, -31.67 \rangle$	$\langle -85.84, -32.41 \rangle$	$\langle -89.73, -34.58 \rangle$	$\langle -90, -34.96 \rangle$	$\langle -90, -34.95 \rangle$
\tilde{f}_1 , Hz	710.63	739.16	713.76	117.25	118.36	117.40
f_1 , Hz	717.03	751.76	720.08	118.01	118.96	118.07
Error, %	-0.89	-1.67	-0.88	-0.64	-0.50	-0.57
κ_{\max} , m^{-1}	1.57	1.57	1.57	1.57	1.57	1.57

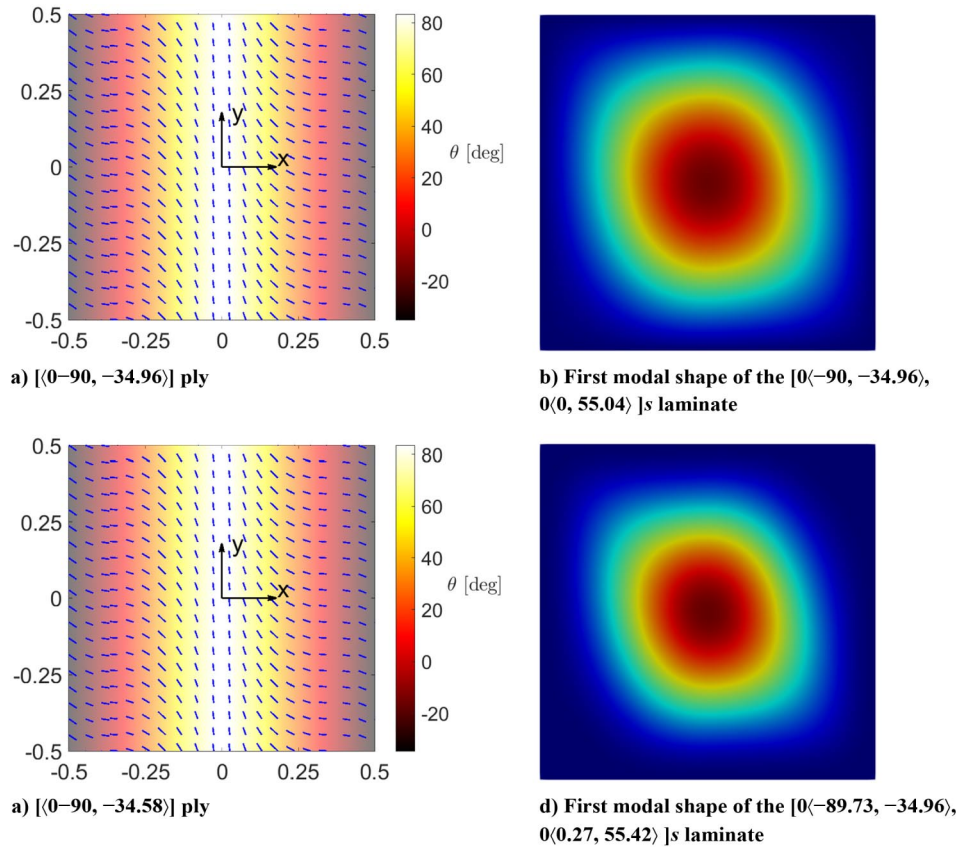


Fig. 13 Fiber paths and first vibration mode of the LW optimum solution for the constrained fundamental frequency optimization problem for thick (a, b) and thin (c, d) laminates.

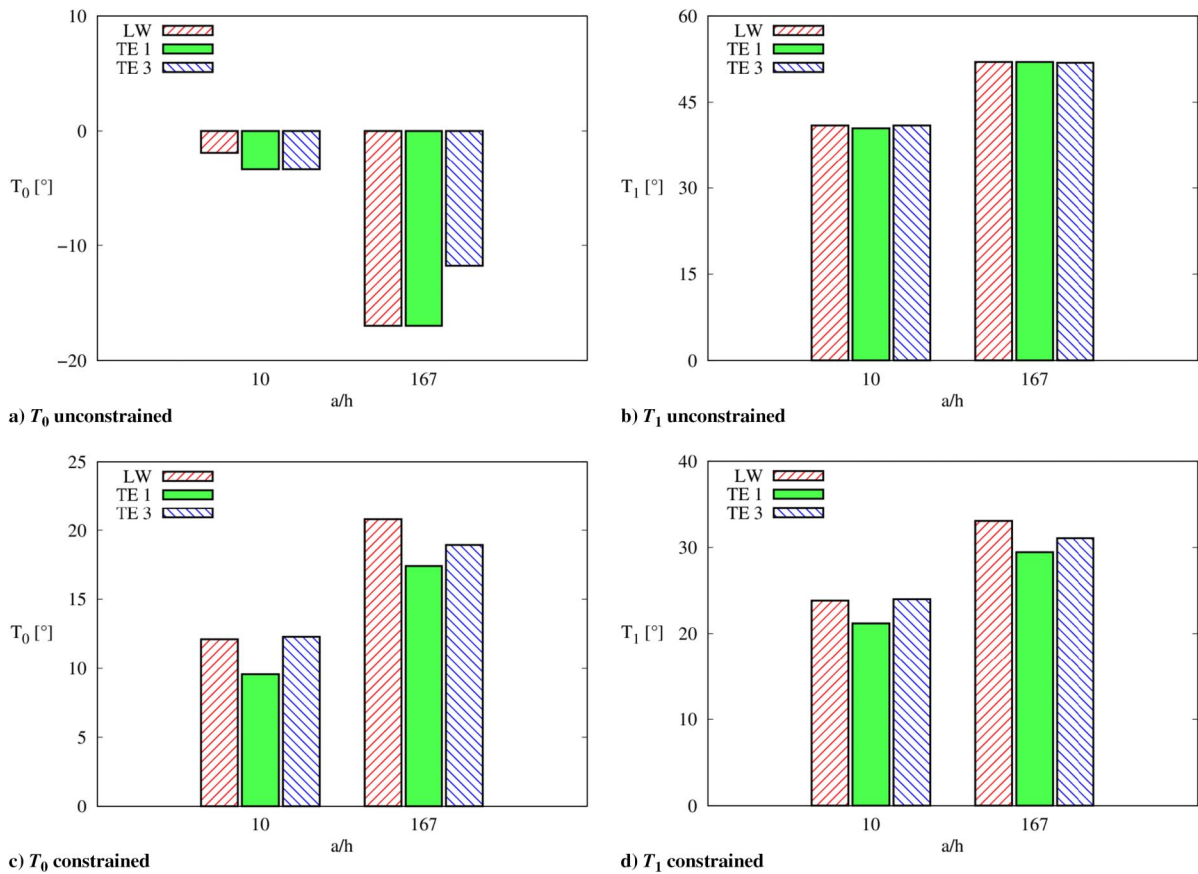


Fig. 14 Histograms gathering the optimal design variables for the unconstrained and constrained buckling optimization problems for the different width-to-thickness ratios a/h and structural theories.

ESL-TE 1. It is worth noting that the solutions to the constrained problem lay on the constraint boundary, as occurred in the buckling optimization problem. Finally, the fiber patterns of the constrained LW solutions for thick and thin laminates are represented in Fig. 13 with their respective first vibration modes.

VI. Conclusions

This paper dealt with the unconstrained and constrained optimization of VAT plates. The VSC structures were modeled by means of ESL and LW CUF-based models. After the verification against literature results of both the buckling load and fundamental frequency, an LHS

sampling strategy was used to generate the input that provided the aforementioned magnitudes as an outcome of the FE simulations. Surrogate models based on polynomial expressions were built using the problem input-output and employed to mimic the buckling load and fundamental frequency, which served as the objective function of the optimization problem. GA was utilized to provide the optimum design variables.

According to the results shown in this paper, the following comments can be made:

1) When optimizing the buckling load of VAT plates, ESL models led to similar results in terms of buckling load and design variables as those obtained with an LW theory in the case of thick and thin plates,

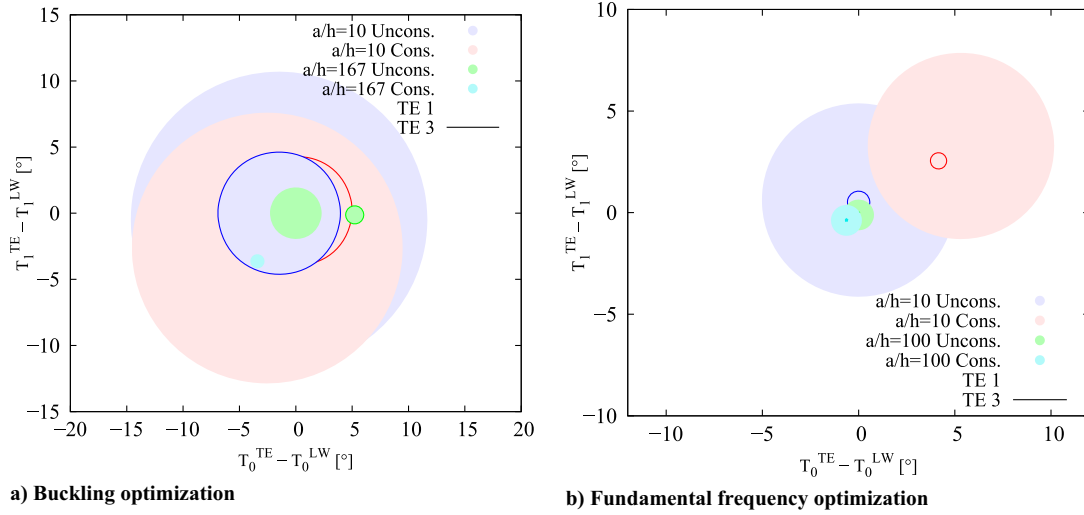


Fig. 15 Absolute error between the optimal $\langle T_0, T_1 \rangle$ obtained by ESL approaches with respect to those retrieved by an LW model. The radius of the circles represents the relative error between the actual simulations using the ESL models with respect to LW.

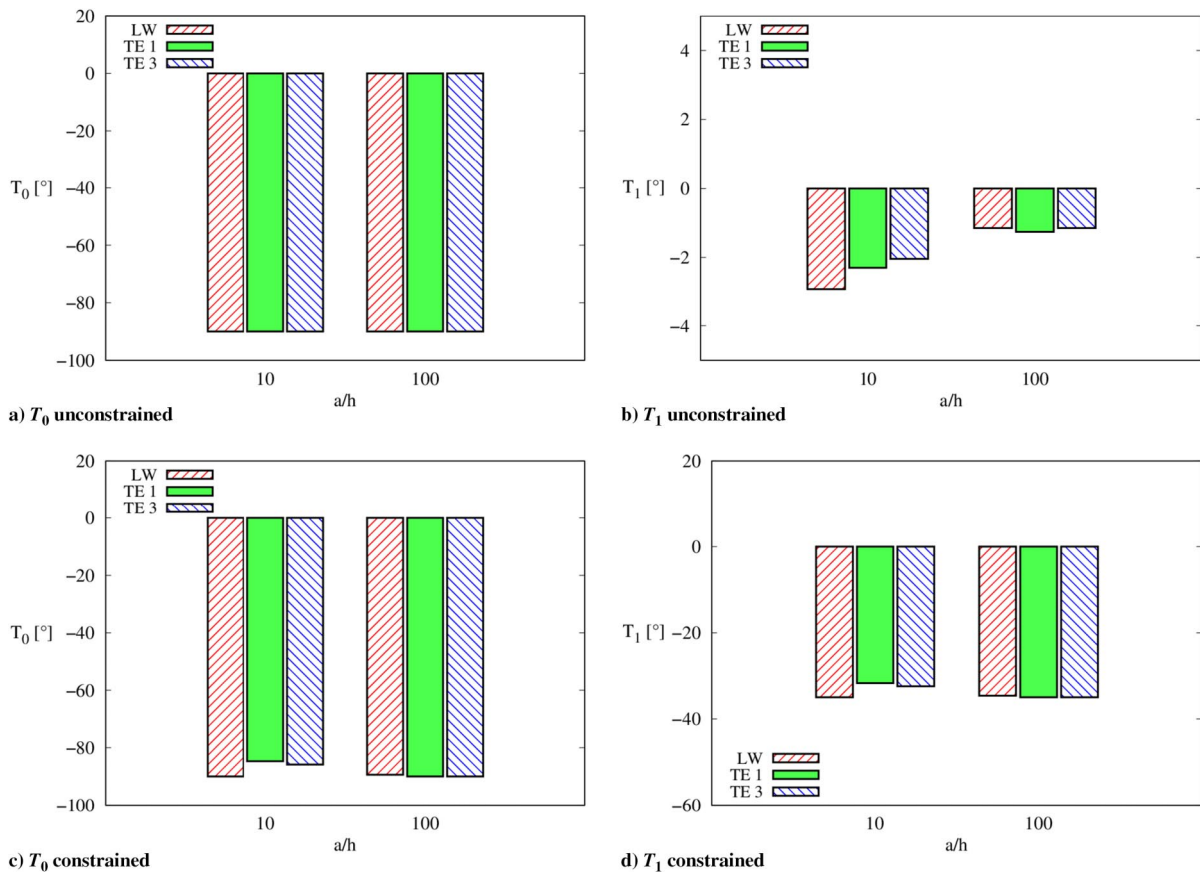


Fig. 16 Histograms gathering the optimal design variables for the unconstrained and constrained fundamental frequency optimization problems for the different width-to-thickness ratios a/h and structural theories.

for both unconstrained and constrained optimization problems, as shown in Fig. 14. In this regard, ESL approaches should be preferable when optimizing the buckling load of VAT plates since they need lower DOF than its LW counterparts. Nevertheless, ESL will overestimate the buckling load since they lead to stiffer models. This is displayed in Fig. 15a, where larger circles are appreciated for the ESL models, especially ESL-TE 1.

2) When optimization of the fundamental frequency is faced, it has been shown that ESL models lead to similar optimal solutions for both unconstrained and constrained problems, as well as width-to-thickness ratios. This is appreciated in Fig. 16. In the case of thin plates, an ESL approach is advantageous compared to LW models since lower DOF are needed to obtain similar values of both the optimal design variables and fundamental frequency, as appreciated in Fig. 15b. However, despite providing similar, if not identical, optimal design variables, ESL-TE 1 models overestimate the frequency by roughly 40 Hz due to the higher stiffness this model leads to.

3) Surrogate models are helpful in solving optimization problems because of the quick evaluation of the objective function/constraints that they mimic. Moreover, if few design variables are considered, a graphical representation of the response surfaces can help predicting the region where the optimum might be located (see Figs. 7b,7d, and 11b). However, errors might be committed if not enough samples are used to build such surrogates or if a lousy sampling strategy is followed; i.e., some regions of the design space are unexplored. This might represent an essential issue if failure constraints or uncertainty are considered in the optimization problem. In those cases, an optimization that uses the results from the actual simulation might be preferred.

Future investigations will account for the manufacturing defects that arise during the fabrication of VAT structures, such as gaps and overlaps, and will face the minimization of stress concentration factors in open-hole composite structures. In the latter case, LW models might lead to different optimal solutions when compared with ESL approaches. Because LW theories provide the kinematic variables of each independent layer, they can predict the 3D stress state of the laminated structure. Precisely, they can capture the shear and normal transverse stresses guaranteeing the C_z^0 requirements. ESL cannot predict the aforementioned stresses, nor guarantee the C_z^0 requirements unless very high order is employed. In that case, the increase in terms of DOF could be disadvantageous if compared to an LW approach.

Acknowledgment

This work is part of a project that has received funding from the European Research Council under the European Union's Horizon 2020 research and innovation program (Grant Agreement No. 850437).

References

- [1] Grimshaw, M., Grant, C., and Diaz, J., "Advanced Technology Tape Laying for Affordable Manufacturing of Large Composite Structures," *International Sample Symposium and Exhibition*, Vol. 46, Citeseer, 2001, pp. 2484–2494, <https://www.scopus.com/inward/record.uri?eid=2-s2.0-0034831640&partnerID=40&md5=ac3eda68699dcda56430f89bc1d2848c>.
- [2] Leissa, A., and Martin, A., "Vibration and Buckling of Rectangular Composite Plates with Variable Fiber Spacing," *Composite Structures*, Vol. 14, No. 4, 1990, pp. 339–357. [https://doi.org/10.1016/0263-8223\(90\)90014-6](https://doi.org/10.1016/0263-8223(90)90014-6)
- [3] Gürdal, Z., and Olmedo, R., "In-Plane Response of Laminates with Spatially Varying Fiber Orientations-Variable Stiffness Concept," *AIAA Journal*, Vol. 31, No. 4, 1993, pp. 751–758. <https://doi.org/10.2514/3.11613>
- [4] Gürdal, Z., Tatting, B. F., and Wu, C., "Variable Stiffness Composite Panels: Effects of Stiffness Variation on the In-Plane and Buckling Response," *Composites Part A: Applied Science and Manufacturing*, Vol. 39, No. 5, 2008, pp. 911–922. <https://doi.org/10.1016/j.compositesa.2007.11.015>
- [5] Raju, G., Wu, Z., Kim, B., and Weaver, P., "Prebuckling and Buckling Analysis of Variable Angle Tow Plates with General Boundary Conditions," *Composite Structures*, Vol. 94, No. 9, 2012, pp. 2961–2970. <https://doi.org/10.1016/j.compstruct.2012.04.002>
- [6] Reissner, E., "The Effect of Transverse Shear Deformation on the Bending of Elastic Plates," *Journal of Applied Mechanics*, Vol. 12, No. 2, 1945, pp. 69–77. <https://doi.org/10.1115/1.4009435>
- [7] Mindlin, R., "Influence of Rotary Inertia and Shear Flexural Motion of Isotropic, Elastic Plates," *Journal of Applied Mechanics*, Vol. 18, No. 1, 1951, pp. 31–38. <https://doi.org/10.1115/1.4010217>
- [8] Akhavan, H., and Ribeiro, P., "Natural Modes of Vibration of Variable Stiffness Composite Laminates with Curvilinear Fibers," *Composite Structures*, Vol. 93, No. 11, 2011, pp. 3040–3047. <https://doi.org/10.1016/j.compstruct.2011.04.027>
- [9] Reddy, J., "A Refined Nonlinear Theory of Plates with Transverse Shear Deformation," *International Journal of Solids and Structures*, Vol. 20, No. 9, 1984, pp. 881–896. [https://doi.org/10.1016/0020-7683\(84\)90056-8](https://doi.org/10.1016/0020-7683(84)90056-8)
- [10] Venkatachari, A., Natarajan, S., and Ganapathi, M., "Variable Stiffness Laminated Composite Shells-Free Vibration Characteristics Based on Higher-Order Structural Theory," *Composite Structures*, Vol. 188, March 2018, pp. 407–414. <https://doi.org/10.1016/j.compstruct.2018.01.025>
- [11] Hao, P., Liu, X., Wang, Y., Liu, D., Wang, B., and Li, G., "Collaborative Design of Fiber Path and Shape for Complex Composite Shells Based on Isogeometric Analysis," *Computer Methods in Applied Mechanics and Engineering*, Vol. 354, Sept. 2019, pp. 181–212. <https://doi.org/10.1016/j.cma.2019.05.044>
- [12] Haftka, R. T., and Walsh, J. L., "Stacking-Sequence Optimization for Buckling of Laminated Plates by Integer Programming," *AIAA Journal*, Vol. 30, No. 3, 1992, pp. 814–819. <https://doi.org/10.2514/3.10989>
- [13] Le Riche, R., and Haftka, R. T., "Optimization of Laminate Stacking Sequence for Buckling Load Maximization by Genetic Algorithm," *AIAA Journal*, Vol. 31, No. 5, 1993, pp. 951–956. <https://doi.org/10.2514/3.11710>
- [14] Le Riche, R., and Haftka, R., "Improved Genetic Algorithm for Minimum Thickness Composite Laminate Design," *Composites Engineering*, Vol. 5, No. 2, 1995, pp. 143–161. [https://doi.org/10.1016/0961-9526\(95\)90710-S](https://doi.org/10.1016/0961-9526(95)90710-S)
- [15] Irisarri, F., Lasseigne, A., Leroy, F., and Le Riche, R., "Optimal Design of Laminated Composite Structures with Ply Drops Using Stacking Sequence Tables," *Composite Structures*, Vol. 107, Jan. 2014, pp. 559–569. <https://doi.org/10.1016/j.compstruct.2013.08.030>
- [16] Fukunaga, H., and Sekine, H., "Stiffness Design Method of Symmetric Laminates Using Lamination Parameters," *AIAA Journal*, Vol. 30, No. 11, 1992, pp. 2791–2793. <https://doi.org/10.2514/3.11304>
- [17] Silva, G., do Prado, A. P., Cabral, P. H., De Breuker, R., and Dillinger, J., "Tailoring of a Composite Regional Jet Wing Using the Slice and Swap Method," *Journal of Aircraft*, Vol. 56, No. 3, 2019, pp. 990–1004. <https://doi.org/10.2514/1.C035094>
- [18] Serhat, G., and Basdogan, I., "Lamination Parameter Interpolation Method for Design of Manufacturable Variable-Stiffness Composite Panels," *AIAA Journal*, Vol. 57, No. 7, 2019, pp. 3052–3065. <https://doi.org/10.2514/1.J057902>
- [19] Nik, M. A., Fayazbakhsh, K., Pasini, D., and Lessard, L., "Surrogate-Based Multi-Objective Optimization of a Composite Laminate with Curvilinear Fibers," *Composite Structures*, Vol. 94, No. 8, 2012, pp. 2306–2313. <https://doi.org/10.1016/j.compstruct.2012.03.021>
- [20] Nik, M. A., Fayazbakhsh, K., Pasini, D., and Lessard, L., "Optimization of Variable Stiffness Composites with Embedded Defects Induced by Automated Fiber Placement," *Composite Structures*, Vol. 107, Jan. 2014, pp. 160–166. <https://doi.org/10.1016/j.compstruct.2013.07.059>
- [21] Vijayachandran, A. A., Davidson, P., and Waas, A. M., "Optimal Fiber Paths for Robotically Manufactured Composite Structural Panels," *International Journal of Non-Linear Mechanics*, Vol. 126, Nov. 2020, Paper 103567. <https://doi.org/10.1016/j.ijnonlinmec.2020.103567>
- [22] Singh, K., and Kapania, R., "Optimal Design of Tow-Steered Composite Laminates with Curvilinear Stiffeners," *2018 AIAA/ASCE/AHS/ASC Structures, Structural Dynamics, and Materials Conference*, AIAA Paper 2018-2243, 2018. <https://doi.org/10.2514/6.2018-2243>
- [23] Zhao, W., and Kapania, R. K., "Buckling Analysis and Optimization of Stiffened Variable Angle Tow Laminates with a Cutout Considering Manufacturing Constraints," *Journal of Composites Science*, Vol. 6,

- No. 3, 2022, p. 80.
<https://doi.org/10.3390/jcs6030080>
- [24] Carvalho, J., Sohoul, A., and Suleman, A., “Fundamental Frequency Optimization of Variable Angle Tow Laminates with Embedded Gap Defects,” *Journal of Composites Science*, Vol. 6, No. 2, 2022, p. 64.
<https://doi.org/10.3390/jcs6020064>
- [25] Carrera, E., Cinefra, M., Petrolo, M., and Zappino, E., *Finite Element Analysis of Structures Through Unified Formulation*, Wiley, Hoboken, NJ, 2014, Chap. 6.
<https://doi.org/10.1002/9781118536643>
- [26] Pagani, A., Enea, M., and Carrera, E., “Quasi-Static Fracture Analysis by Coupled Three-Dimensional Peridynamics and High Order One-Dimensional Finite Elements Based on Local Elasticity,” *International Journal for Numerical Methods in Engineering*, Vol. 123, No. 4, 2022, pp. 1098–1113.
<https://doi.org/10.1080/15376494.2022.2098430>
- [27] Shen, J., Arruda, M., and Pagani, A., “Concrete Damage Analysis Based on Higher-Order Beam Theories Using Fracture Energy Regularization,” *Mechanics of Advanced Materials and Structures*, 2022.
<https://doi.org/10.1080/15376494.2022.2098430>
- [28] Demasi, L., Biagini, G., Vannucci, F., Santarpia, E., and Cavallaro, R., “Equivalent Single Layer, Zig-Zag, and Layer Wise Theories for Variable Angle Tow Composites Based on the Generalized Unified Formulation,” *Composite Structures*, Vol. 177, Oct. 2017, pp. 54–79.
<https://doi.org/10.1016/j.compstruct.2017.06.033>
- [29] Viglietti, A., Zappino, E., and Carrera, E., “Analysis of Variable Angle Tow Composites Structures Using Variable Kinematic Models,” *Composites Part B: Engineering*, Vol. 171, Aug. 2019, pp. 272–283.
<https://doi.org/10.1016/j.compositesb.2019.03.072>
- [30] Sánchez-Majano, A. R., Azzara, R., Pagani, A., and Carrera, E., “Accurate Stress Analysis of Variable Angle Tow Shells by High-Order Equivalent-Single-Layer and Layer-Wise Finite Element Models,” *Materials*, Vol. 14, No. 21, 2021, p. 6486.
<https://doi.org/10.3390/ma14216486>
- [31] Pagani, A., Azzara, R., and Carrera, E., “Geometrically Nonlinear Analysis and Vibration of In-Plane-Loaded Variable Angle Tow Composite Plates and Shells,” *Acta Mechanica*, Vol. 4, May 2022, pp. 1–24.
<https://doi.org/10.1007/s00707-022-03226-2>
- [32] Pagani, A., and Sánchez-Majano, A. R., “Stochastic Stress Analysis and Failure Onset of Variable Angle Tow Laminates Affected by Spatial Fibre Variations,” *Composites Part C: Open Access*, Vol. 4, March 2021, Paper 100091.
<https://doi.org/10.1016/j.jcomc.2020.100091>
- [33] Sánchez-Majano, A. R., Pagani, A., Petrolo, M., and Zhang, C., “Buckling Sensitivity of tow-Steered Plates Subjected to Multiscale Defects by High-Order Finite Elements and Polynomial Chaos Expansion,” *Materials*, Vol. 14, No. 11, 2021, p. 2706.
<https://doi.org/10.3390/ma14112706>
- [34] Brooks, T., and Martins, J., “On Manufacturing Constraints for Tow-Steered Composite Design Optimization,” *Composite Structures*, Vol. 204, Nov. 2018, pp. 548–559.
<https://doi.org/10.1016/j.compstruct.2018.07.100>
- [35] Carrera, E., “Theories and Finite Elements for Multilayered, Anisotropic, Composite Plates and Shells,” *Archives of Computational Methods in Engineering*, Vol. 9, No. 2, 2002, pp. 87–140.
<https://doi.org/10.1007/BF02736649>
- [36] Pagani, A., Yan, Y., and Carrera, E., “Exact Solutions for Static Analysis of Laminated, Box and Sandwich Beams by Refined Layer-Wise Theory,” *Composites Part B: Engineering*, Vol. 131, Dec. 2017, pp. 62–75.
<https://doi.org/10.1016/j.compositesb.2017.08.001>
- [37] Wu, B., Pagani, A., Chen, W., and Carrera, E., “Geometrically Non-linear Refined Shell Theories by Carrera Unified Formulation,” *Mechanics of Advanced Materials and Structures*, Vol. 28, No. 16, 2019, pp. 1721–1741.
<https://doi.org/10.1080/15376494.2019.1702237>
- [38] Carrera, E., “CZ0 Requirements: Models for the Two Dimensional Analysis of Multilayered Structures,” *Composite Structures*, Vol. 37, Nos. 3–4, 1997, pp. 373–383.
[https://doi.org/10.1016/S0263-8223\(98\)80005-6](https://doi.org/10.1016/S0263-8223(98)80005-6)
- [39] Marques, F., Mota, A., and Loja, M., “Variable Stiffness Composites: Optimal Design Studies,” *Journal of Composites Science*, Vol. 4, No. 2, 2020, p. 80.
<https://doi.org/10.3390/jcs4020080>
- [40] Zhao, W., Singh, K., and Kapania, R. K., “Thermal Buckling Analysis and Optimization of Curvilinearly Stiffened Plates with Variable Angle Tow Laminates,” *Journal of Spacecraft and Rockets*, Vol. 56, No. 4, 2019, pp. 1189–1204.
<https://doi.org/10.2514/1.A34378>
- [41] Darwin, C., *On the Origin of Species*, 1859, Routledge, Oxfordshire, England, U.K., 2004, Chap. 4.
<https://doi.org/10.4324/9780203509104>
- [42] Montemurro, M., Vannucci, P., and Vincenti, A., *BIANCA, A Genetic Algorithm for Engineering Optimisation-User Guide*, 2011, <https://hal.science/hal-00767468/file/UserGuide.pdf>.
- [43] Gary Wang, G., and Shan, S., “Review of Metamodeling Techniques in Support of Engineering Design Optimization,” *Journal of Mechanical Design*, Vol. 129, No. 4, 2007, pp. 370–380.
<https://doi.org/10.1115/1.2429697>
- [44] Ghanem, R., and Spanos, P., *Stochastic Finite Elements: A Spectral Approach*, Springer, New York, 1991, Chap. 2.4.
<https://doi.org/10.1007/978-1-4612-3094-6>
- [45] Krishnamurthy, T., “Response Surface Approximation with Augmented and Compactly Supported Radial Basis Functions,” *44th AIAA/ASME/ASCE/AHS/ASC Structures, Structural Dynamics, and Materials Conference*, AIAA Paper 2003-1748, 2003.
<https://doi.org/10.2514/6.2003-1748>
- [46] Sacks, J., Welch, W. J., Mitchell, T. J., and Wynn, H. P., “Design and Analysis of Computer Experiments,” *Statistical Science*, Vol. 4, No. 4, 1989, pp. 409–423.
<https://doi.org/10.1214/ss/1177012413>
- [47] Forrester, A., and Keane, A., “Recent Advances in Surrogate-Based Optimization,” *Progress in Aerospace Sciences*, Vol. 45, Nos. 1–3, 2009, pp. 50–79.
<https://doi.org/10.1016/j.paerosci.2008.11.001>
- [48] McKay, M., Beckman, R., and Conover, W., “A Comparison of Three Methods for Selecting Values of Input Variables in the Analysis of Output from a Computer Code,” *Technometrics*, Vol. 42, No. 1, 2000, pp. 55–61.
<https://doi.org/10.1080/00401706.2000.10485979>
- [49] Carrera, E., Cinefra, M., and Nali, P., “MITC Technique Extended to Variable Kinematic Multilayered Plate Elements,” *Composite Structures*, Vol. 92, No. 8, 2010, pp. 1888–1895.
<https://doi.org/10.1016/j.compstruct.2010.01.009>
- [50] Olmedo, R., and Gürdal, Z., “Buckling Response of Laminates with spatially varying fiber orientations,” *34th Structures, Structural Dynamics and Materials Conference*, AIAA Paper 1993-1567, 1993.
<https://doi.org/10.2514/6.1993-1567>

R. Ohayon
Associate Editor